Tuning microporosity and surface chemistry: The synergistic effect of KOH and urea on CO capture performance of sucrose-derived activated carbons

Original
Tuning microporosity and surface chemistry: The synergistic effect of KOH and urea on CO capture performance of sucrose-derived activated carbons / Etzi, M., Sartoretti, E., Bensaid, S., Allione, M., Ferraris, S., Castellino, M., Armandi, M.. - In: CHEMICAL ENGINEERING JOURNAL. - ISSN 1385-8947. - 521:(2025), pp. 1-17. [10.1016/j.cej.2025.167166]

Availability:
This version is available at: 11583/3008400 since: 2026-03-10T14:08:59Z

Publisher:
Elsevier

Published
DOI:10.1016/j.cej.2025.167166

Chemical Engineering Journal 521 (2025) 167166

Contents lists available at ScienceDirect

Chemical Engineering Journal

journal homepage: www.elsevier.com/locate/cej

Tuning microporosity and surface chemistry: The synergistic effect of KOH and urea on CO_2 capture performance of sucrose-derived activated carbons

Marco Etzi [a], Enrico Sartoretti [b], Samir Bensaid [b], Marco Allione [b], Sara Ferraris [b], Micaela Castellino [a,b], Marco Armandi [b,*]

[a] Center for Sustainable Future Technologies@Polito, Istituto Italiano di Tecnologia, Via Livorno 60, 10144 Torino, Italy
[b] Department of Applied Science and Technology (DISAT), Politecnico di Torino, Corso Duca degli Abruzzi 24, 10129 Torino, Italy

ARTICLE INFO

Keywords:
Sucrose
Porous activated carbon
Activating agent
CO_2 Adsorption

ABSTRACT

The optimization of activated carbons (ACs) for CO_2 adsorption is a critical challenge in carbon capture technologies, and a precise control over porosity and surface chemistry is needed to develop high-performance ACs. This study explores the effects of activation conditions on the microporosity and surface chemistry of ACs derived from sucrose, highlighting the synergistic role of KOH and urea in a one-step activation process. The combined use of KOH and urea significantly enhances CO_2 uptake (up to 7.36 mmol g^{-1} at 0 °C and 740 Torr) by promoting the formation of ultra-micropores (<0.7 nm) and incorporating N- and K-based adsorption sites. Furthermore, urea plays a crucial role in preventing the formation of residual potassium carbonate occurring for activation temperature $\leq$ 700 °C, thereby improving the efficiency of KOH activation at low activation temperature and ensuring a well-developed porous network favourable for CO_2 capture. KOH/urea activated carbons show a CO_2:N_2 selectivity of up to 61 at 20 °C in a 15:85 CO_2:N_2 mixture, outperforming the materials activated using KOH-only in post-combustion conditions. These findings provide fundamental insights into the mechanisms governing KOH/urea co-activation and offer a scalable, cost-effective strategy for designing high-performance ACs in industrial CO_2 capture applications.

1. Introduction

Carbon capture and utilization represents a viable solution to mitigate rising greenhouse gas concentrations. Fossil fuel combustion is considered a major contributor to atmospheric CO_2 accumulation; therefore, various strategies can be applied to capture CO_2 in post-combustion flue gases, such as amine scrubbing, membrane separation, and solid sorbent adsorption. This latter technology offers the advantages of low preparation and regeneration costs, ease of use, and the absence of corrosion. Different classes of solid sorbents have been used for CO_2 adsorption, including zeolites, metal-organic frameworks (MOFs), and porous activated carbons (ACs). ACs have attracted wide attention due to their easy synthesis, tunable porosity, high hydrophobicity, and low cost. ACs are typically prepared through physical or chemical activation of raw materials, such as biomass, coke, resins, *etc.* Chemical activation generally yields ACs with enhanced microporosity, while physical activation typically produces materials with a higher proportion of mesopores [1]. Significant efforts have been spent to synthesize chemically activated ACs characterized by narrow microporosity, since ultra-micropores (*i.e.* pores smaller than 0.7 nm) are known to be more efficient in capturing CO_2, leading to higher CO_2 density in the adsorbed phase [2–4].

In designing a procedure for the preparation of ACs for CO_2 capture, the choice of the carbon precursor is undoubtedly a key factor that must ensure the cost-effectiveness of the process. Cheap biomass (*e.g.* rice husk, coconut shell, *etc.*) is extensively used as a carbon precursor in the preparation of ACs, but generally requires a two-step high-temperature process [5–9]. The first step involves the pyrolysis of biomass at $T =$ 500–900 °C under an inert gas leading to a biochar; in the second step, the resulting biochar is mixed with chemically activating agents (*e.g.* KOH [7] or H_3PO_4 [9]) and heated under inert atmosphere at $T =$ 600–1000 °C. On the other hand, various polysaccharides can be used as precursors in one-step syntheses, which at most involve a preliminary low-temperature dehydration, leading to a significant reduction in energy costs [10–13]. Actually, catalytic low-temperature dehydration of sucrose has proved an effective strategy for the preparation of a carbon-

---

[*] Corresponding author.
E-mail address: marco.armandi@polito.it (M. Armandi).

https://doi.org/10.1016/j.cej.2025.167166
Received 14 April 2025; Received in revised form 1 August 2025; Accepted 11 August 2025

rich precursor suitable for chemical activation [14–16].

As for activating agents, KOH is probably one of the most used [5,17–20]. For instance, He et al. [5] used KOH and chitosan to activate a biochar previously obtained by carbonization of rice husk; the reported CO_2 uptake at 0 °C and 760 Torr was 5.83 mmol g^{-1}. Wang et al. [17] showed that activation with KOH of pyrolyzed celtuce leaves yields an AC with remarkable CO_2 adsorption at 760 Torr (6.04 mmol g^{-1} at 0 °C). KOH activation at pre-carbonized cupuassu shells led to microporous-activated carbon showing outstanding CO_2 uptake at 760 Torr (4.4 and 7.8 mmol g^{-1} at 25 °C and 0 °C, respectively) [18]. Even more interestingly, Li et al. described a novel synthesis method involving autogenic pressure carbonization and KOH activation for the preparation of porous carbon derived from polyethylene terephthalate (PET) waste, achieving exceptional CO_2 uptake at 760 Torr (4.44 mmol g^{-1} at 25 °C) [19].

The fundamental processes involved in KOH activation, and their dependence on synthesis variables (*e.g.* nature of the precursor, KOH/precursor ratio, activation temperature, sweep gas flow rates) have been widely investigated [21–24]. The generally accepted mechanism consists of several reactions that become spontaneous at different temperatures. The reaction between KOH and the precursor starts at $T > 570\ ^\circ C$ according to reactions (1) and (2):

$$6\ KOH_{(l)} + 2C_{(s)} \rightarrow 2\ K_{(l)} + 3H_{2(g)} + 2K_2CO_{3(s)} \tag{1}$$

$$4\ KOH_{(l)} + 2CH_{X(s)} \rightarrow K_2O_{(s)} + \left(2 + \frac{x}{2}\right)H_{2(g)} + K_2CO_{3(s)} \tag{2}$$

$T > 700\ ^\circ C$ are required for the reaction of K_2CO_3 and K_2O with the carbon matrix, according to Eqs. (3)–(5):

$$K_2CO_{3(s)} \rightarrow K_2O_{(s)} + CO_{2(g)} \tag{3}$$

$$K_2CO_{3(s)} + 2C_{(s)} \rightarrow 2\ K_{(l)} + 3CO_{(g)} \tag{4}$$

$$2K_2O + C_{(s)} \rightarrow 2\ K_{(l)} + CO_{(g)} \tag{5}$$

It is widely recognized that the intercalation of metallic K — generated through reactions (1)–(5) — into the spaces between graphene layers plays a crucial role in the porosity development in various carbon materials [25–27]. During activation, metallic K can penetrate the carbon matrix and transfer an electron to the carbon's π-electronic network, leading to the formation of donor-type graphite intercalation compounds [26]. The intercalated K could be also associated with oxygen functionalities within the carbon matrix *via* the formation of quasi-chemical bonds of the C-O-K type [25]. The role of intercalated K in enhancing both CO_2 adsorption uptake and strength is not always fully considered [28]. Indeed, several activation procedures include a thorough final washing step with HCl solution, mainly aimed at removing impurities (*e.g.* K_2CO_3) generated during the process [4,13–15]. This washing step is often essential for optimizing the ACs porous properties, but it may also remove some framework K species responsible for electrostatic interaction of the carbon surface with CO_2 [25].

Several non-metals such as N, S, and P have also been investigated as heteroatoms capable of enhancing the adsorptive properties of ACs [8,13,31,32]. For instance, N and S co-doped porous carbons derived from phenol-formaldehyde resin showed exceptional potential for selective CO_2 capture [31]. One of the most common strategies to enhance CO_2-AC interactions is to increase the basicity of the carbon framework by introducing N-heteroatoms, which can anchor the electron-deficient carbon atom of CO_2 through Lewis acid-base interactions. In particular, pyridinic and pyrrolic groups are often considered the most effective N functionalities for enhancing CO_2 adsorption properties, as they exhibit a Lewis basic character (pyridinic-N donates one electron to aromatic π-system while pyrrolic-N offers 2p -electrons) [33,34]. In this context, urea is one of the most common N-dopants used to prepare N-enriched precursors, which, in turn, are activated with a chemical agent [11,35–38]. One-step processes involving only one high-temperature thermal treatment are however desirable given their lower preparation cost and easy scalability [30,39].

In this work, we investigated the activation of sucrose-derived char for the preparation of ACs with enhanced CO_2 adsorption uptake. First, we optimized the KOH-to-char (K/C) ratio to achieve an optimal micropore size distribution, then explored the combined KOH/urea activation to introduce both K- and N-surface moieties into the resulting ACs. Unlike previous studies, which typically rely on two-step processes or pre-carbonized biomass, this work demonstrates a simple and scalable one-step synthesis starting from sucrose, achieving high CO_2 uptake while preserving surface functionalities relevant to adsorption performance**.** The role of these species in enhancing the interaction energy, CO_2/N_2 selectivity, and CO_2 uptake was demonstrated. Importantly, we provide evidence for the role of residual K-based species in enhancing CO_2 affinity, a contribution often underestimated in the literature due to their removal during acid washing treatments commonly applied to optimize textural properties. This work provides significant insights into the KOH and urea activation mechanisms in a one-pot synthesis, offering a deeper understanding of the complex interactions that govern the process.

2. Materials and methods

2.1. Synthesis of ACs

2.1.1. Preparation of the char

A Petri dish containing an aqueous solution obtained by mixing 10 mL Milli-Q water, 5 g sucrose (Merck, ≥ 99.5 %), and 20 μL sulfuric acid (Fluka 95–97 %) was placed into an oven, and kept first at 100 °C (3 h) and then at 160 °C (3 h). This thermal treatment follows a typical procedure reported in the literature [40], in which the initial heating at 100 °C favours the concentration of the reaction mixture, while the subsequent step at 160 °C induces catalytic dehydration of sucrose. The obtained char (about 2.5 g), hereinafter referred to as CS, was ground in an agate mortar and used for the following preparations.

2.1.2. Synthesis of the CS-X and CS-KX series

A portion of CS was directly pyrolyzed in a tubular furnace under N_2 flow (flow rate: 500 mL/min; heating rate: 10 °C min^{-1}) at 600, 700, or 800 °C, yielding a set of non-activated samples (CS-X, where X = 6, 7, or 8 for T = 600, 700, and 800 °C, respectively). Low burn-off were measured for these samples (*i.e.* 10–15 wt%). For the preparation of the *CS-KX series*, the char was soaked into KOH solutions, with KOH to char weight ratios (hereafter indicated with the notation K/C) equal to 0.5, 1.0, and 1.5. After evaporation, the samples were carbonized at different activation temperatures T_{act} (X = 6, 7, or 8 for T_{act} = 600, 700 and 800 °C, respectively) under N_2 flow (flow rate 500 mL/min, heating rate 10 °C min^{-1}). The resultant ACs were washed with *ca.* 200 mL Milli-Q water, and dried overnight. Only the most significant results, predominantly related to the samples prepared with K/C = 1.0, are reported in Section 3. Therefore, unless specified otherwise, the acronym *CS-KX* refers to samples prepared with this K/C ratio. Furthermore, one representative sample (CS-K7-W) was washed with HCL 1.0 M to investigate the effect of washing conditions.

2.1.3. Synthesis of the CS-KUX series

For the preparation of the *CS-KUX* samples, the char was soaked into solutions of KOH and urea, with KOH/urea/char weight ratios of 1:1:1. After evaporation, the samples were carbonized at different temperatures (X = 6, 7 or 8 for T_{act} = 600, 700 and 800 °C, respectively) under N_2 flow (flow rate 500 mL/min, heating rate 10 °C min^{-1}). The resultant ACs were washed with *ca.* 200 mL Milli-Q water, and dried overnight. Additional samples were prepared with urea only (CS-U8) or replacing KOH with K_2CO_3 (CS-KCU6 or CS-KCU7). In the latter case, a K_2CO_3/CS ratio of 1.2 was used to ensure the same K amount as in KOH activation.

The burn-off % of all the samples was measured from the initial mass of CS char and the final mass of AC, according to Eq. (6)

$$Burn-off\% = \frac{100 \bullet mass_{(CS)} - 100 \bullet mass_{(AC)}}{mass_{(CS)}} \tag{6}$$

The carbon yield can be readily estimated as the difference between 100 % and the burn-off value.

2.2. Characterization

X-ray Diffraction (XRD) patterns of the powders were measured on an X'Pert Philips diffractometer (PANalytical B.V.), using Cu Kα radiation (λ = 1.5415 Å) in the 10°–60° 2θ range (step width = 0.02° 2θ; time per step 5 s).

Microtopography and chemical composition of the samples were investigated by Field Emission Scanning Electron Microscopy (FESEM). Images were acquired on a Zeiss Merlin microscope with a Gemini-II column. The instrument is equipped with an Energy Dispersive X-ray (EDX) probe used to determine the samples chemical composition by a raster scan of ~ 500 μm^2 of sample surface (the average values of three different areas are reported in Table 1).

High-resolution transmission electron microscopy (HRTEM) images were collected in a Talos F200X (Thermo Fisher Scientific) operated at its maximum acceleration voltage of 200 kV, while Energy dispersive X-ray Spectroscopy (EDX) spectra and maps were obtained in the same machine operated in Scanning transmission electron microscopy (STEM) mode to detect any presence of aggregates or any heterogeneous elemental distribution in the sample. Sample preparation was realized by means of a dual-beam machine combining a focused ion beam (FIB) with a field emission scanning electron microscope (SEM) in the same vacuum chamber. The machine (Solaris X, Tescan) was equipped with a plasma source generating a beam of Xenon ions accelerated at energies up to 30 keV. After cutting a small lamella-shaped portion of the sample from a larger chunk, the portion was transferred and glued to a standard TEM Cu lift-out grid (Omniprobe 3-pins lift-out grids) using the machine-embedded nanomanipulator. All gluing processes were made using ion beam-induced Pt deposition using local decomposition of an organic precursor injected into the dual-beam machine vacuum chamber. Final polishing of the thinned portion was made with a gentler beam, after decreasing Xe ions energy down to 3 keV to minimize eventual damaging and distortion of any eventual crystalline structure in the material.

X-ray Photoelectron Spectroscopy (XPS) measurements were conducted on a PHI 5000 Versaprobe spectrometer equipped with a monochromatic Al Kα (1486.6 eV) X-ray source. An electron gun and an Ar^+ gun were used as charge compensation system. The spot size was 100 μm and the pass energy was set at 187.85 eV and 23.5 eV for the acquisition of survey and high-resolution scans, respectively. The spectra were processed using CasaXPS software (v2.3.23, Casa Software Ltd).

Thermogravimetric analysis (TGA, Mettler Toledo 1600) was run under flowing 50 mL/min synthetic Air. After an initial isothermal step at 25 °C (1 h), samples were heated from 25 to 800 °C with a constant heating ramp of 10 °C min^{-1}.

N_2 (SIAD, 99.9995 % purity) adsorption/desorption isotherms were measured at the nominal temperature of −196 °C (77 K), on *ca.* 100 mg powder sample previously outgassed at 250 °C for 5 h to remove water and other atmospheric contaminants (Micromeritics ASAP 2020Plus). Specific surface area (SSA) was calculated according to the BET (Brunauer-Emmett-Teller) method; the total pore volume (V_{TOT}) was determined from the adsorbed amount at $P/P^0 = 0.98$; micropore volume ($V_{MP(t\text{-}plot)}$) was calculated by applying the *t*-plot method; the pore size distribution was calculated by applying the NLDFT (Non Linear Density Functional Theory) method for carbon slit pores.

Table 1
Elemental composition as measured by EDX. Surface composition as measured by XPS is reported in brackets.

Sample	C (At.%)	O (At.%)	K (At.%)	N (At.%)	S (At.%)
CS-K8	93.6	5.8	0.4	0	0.2
CS-K7	81.4	15.2	3.2	0	0.2
CS-K6	83.9	13.5	2.4	0	0.2
CS-KU8	94.0 (88.2)	3.1 (7.9)	0.4 (1.6)	2.4 (2.4)	0.1
CS-KU7	85.2 (84.7)	9.8 (11.0)	1.8 (1.8)	3.1 (2.5)	0.1
CS-KU6	78.7 (78.2)	11.8 (13.7)	2.2 (2.2)	7.1 (5.9)	0.2

2.3. CO_2 Adsorption measurements

CO_2 (SIAD, 99.995 % purity) adsorption isotherms at 0 °C (273.15 K), 10 °C (283.15 K, only on CS-KU*X* samples), and 20 °C (293.15 K) were measured on *ca.* 100 mg powder sample previously outgassed at 250 °C for 5 h to remove water and other atmospheric contaminants (Micromeritics ASAP 2020Plus equipped with an Iso-controller unit for temperature control). The same instrument and procedure were used to measure N_2 adsorption isotherms at 20 °C, which were employed for Ideal Adsorption Solution Theory (IAST) selectivity determination.

To verify the possible presence of irreversibly adsorbed CO_2, two-run experiments were conducted at 0 °C on the activated sample. After the first adsorption run, the samples were outgassed at room temperature (for 1 h) and subsequently underwent a second adsorption run, in which only reversible physisorption occurs.

CO_2 isotherms at 273.15 K were also used as a probing tool to determine the micropore volumes ($V_{MP(D\text{-}R)}$) using the Dubinin–Radushkevich (D-R) method (Eq. (6)) [41–43].

$$V = V_o exp\left[-\left(\frac{A}{\beta E_o}\right)^2\right] \tag{6}$$

where *V and* V_o are the filled volume and micropore volume determined at a constant temperature (*T*) and a relative pressure (P/P^0), $A = RT \ln (P^0/P)$ and E_0 represent the characteristic energy, and β is the CO_2 affinity coefficient (0.35).

From CO_2 adsorption isotherms recorded at $T_1 = 273.15$ K and $T_2 = 293.15$ K, the corresponding values of isosteric heat of adsorption $Q_{st} = -\Delta H_{ads}$ were obtained through the Clausius–Clapeyron equation (Eq. (7)) [44],

$$\left[\frac{\partial \ln p}{\partial T}\right]_{n_{ads}} = -\frac{\Delta H_{ads}}{RT^2} \tag{7}$$

which, in the present case, assumes the following expression (Eq. (8)):

$$Q_{st}(n_{ads}) = R \bullet \ln\left(\frac{p_2}{p_1}\right)\left(\frac{T_1 \bullet T_2}{T_2 - T_1}\right) = 33.275\ (kJ\ mol^{-1}) \bullet \ln\left(\frac{p_2}{p_1}\right) \tag{8}$$

For the most relevant samples (CS-KU*X*), the isosteric heat of adsorption was calculated using three different temperatures (273.15 K, 283.15 K, and 293.15 K), to ensure reliable results.

CO_2/N_2 adsorption selectivity at 20 °C (for a mixture composition $CO_2:N_2 = 15:85$) was calculated with IAST [45]. The adsorption selectivity is given by Eq. (9):

$$IAST\ Selectivity = \frac{qCO_2/qN_2}{pCO_2/pN_2} \tag{9}$$

where *q* represents the mole fractions of the components in the adsorbed phase, while *p* is used for bulk phase.

The breakthrough flue-gas separation experiments were carried out on a home-made apparatus [46], consisting of a U-shaped quartz reactor equipped with three Brooks 5850S mass flow controllers, a Carbolite TF3 tubular furnace, and an Emerson X-STREAM continuous gas analyser to monitor the CO_2 concentration in the outlet stream. Approximately 200 mg of sample were first degassed under vacuum at 250 °C for

5 h using the degassing station of the ASAP 2020 instrument, to accurately determine the mass of the degassed sample. The sample was then transferred to the quartz reactor and subjected to an additional pretreatment at the same temperature (250 °C) under a N_2 flow of 50 mL/min. After cooling to 30 °C, dynamic CO_2 adsorption was investigated under isothermal conditions at atmospheric pressure. The experiment started by switching the feed gas from pure N_2 to a mixture of 20 % CO_2 in N_2 (20 mL/min). The composition of the outlet stream was monitored until saturation was reached. The dynamic CO_2 uptake of the ACs was calculated by integrating the breakthrough curves after subtraction of dead volumes as determined in blank experiment (*i.e.* integration of measured breakthrough curves on an inert fixed bed under the same conditions).

3. Results

3.1. Materials characterization

3.1.1. X-ray diffraction

The graphitization degree of prepared ACs were analysed by powder X-ray diffraction (XRD), and the obtained patterns are shown in Fig. 1.

The set of samples synthesized without any activating agent (CS-*X*) displays the common pattern of amorphous carbons with a low degree of graphitization [14]. Two broad peaks around 22° and 43° 2θ are observed, corresponding to the reflection of the (002) planes and the overlapping reflections of the (100) and (101) planes of graphite, respectively [47]. The increase in carbonization temperature results in a slightly higher degree of graphitization, as evidenced by the intensification of all the peaks.

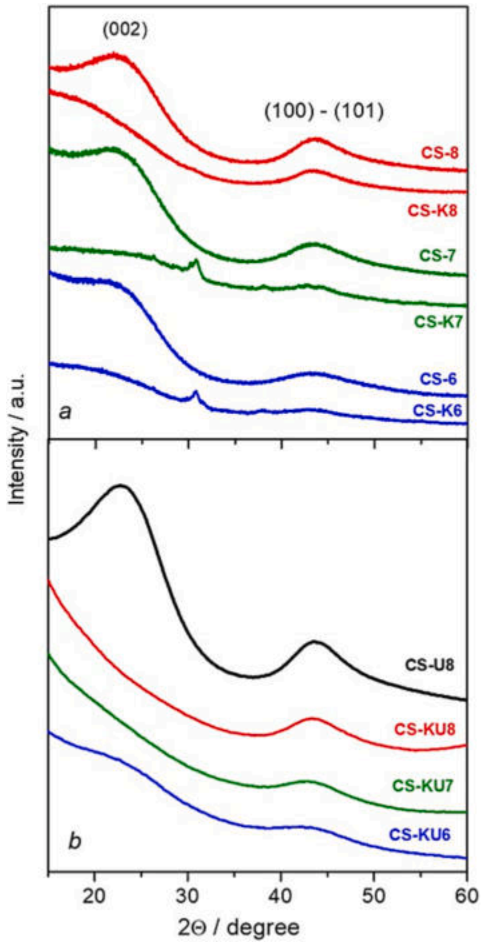

Fig. 1. XRD patterns of CS-*X*, CS-K*X* (a), and CS-KUX (b).

In contrast, activation with KOH (both with and without urea) yields more disordered carbon structures, preventing the growth of the (002) plane, regardless of T_{act}. This behaviour is attributed to the intercalation of metallic K formed in reactions (1)–(5) into the carbon lattice, which consequently hinders the stacking of graphene layers. The patterns of samples activated at 600 °C and 700 °C with KOH only (CS-K6 and CS-K7) show additional peaks in the 28–32° 2θ range, likely due to potassium carbonate (K_2CO_3), hydrogen carbonate ($KHCO_3$), or mixed $K_4H_2(CO_3)_3 \cdot 1.5H_2O$ phases. A precise assignment of these weak and broad peaks to any of the above-mentioned phases is hindered by their overlapping angles. The presence of K-containing phases is due to the reactions between KOH and carbon precursors occurring during the activation, yielding K_2CO_3, K_2O, and K (Eqs. (1) and (2)). Both the decomposition (reaction (3)) and reduction (reaction (4)) of K_2CO_3 require temperatures above 700 °C, and some carbonate may not be efficiently removed during the final washing. Furthermore, K_2O and metallic K require temperatures above 700 °C to react with carbon (Eq. (5)) and to evaporate (boiling temperature $T_{boil(K)} = 759$ °C), respectively. After the removal of the samples from the furnace (*i.e.* upon exposure to air), some residual K_2O and K readily react with CO_2 and H_2O to form $KHCO_3$, K_2CO_3, or mixed phases. Prolonged washing in water (in which all salts are highly soluble) was clearly not sufficient to remove all the K-containing compounds. Even prolonged washing with 1 M HCl solution (sample CS-K7-W) did not lead to the complete removal of these compounds (Fig. S1), suggesting that most of them are embedded within the bulk of the carbon matrix. Diffusion of the solvent into and out of the deeper regions of CS-K6 and CS-K7 particles could be limited by their narrow microporosity, thus hindering the removal of potassium salts. Potassium (hydrogen)carbonates were also observed in samples prepared at 600 and 700 °C with a lower K/C ratio (*i.e.* K/C = 0.5 for CS-K6–0.5 and CS-K7–0.5, XRD not shown). At the same time, these results discouraged us from investigating K/C ratios >1 for these activation temperatures. On the other hand, no additional phases were observed for sample CS-K8. Indeed, at $T_{act} = 800$ °C, both K_2CO_3 and K_2O are reduced to metallic K, which evaporates and is removed from the carbon structure. The same behaviour was observed even adopting a higher K/C ratio for the activation at 800 °C (*i.e.* K/C = 1.5 in sample CS-K8–1.5, Fig. S2), indicating that at this T_{act}, a higher amount of KOH can be used for activation without leading to salt residues.

Interestingly, XRD patterns of all samples activated with KOH and urea do not exhibit any peaks corresponding to K-containing compounds. A plausible explanation for this behaviour is the reaction between urea and K_2CO_3, which leads to the formation of KOCN and $(NH_4)_2CO_3$. The latter further decomposes into NH_3, H_2O, and CO, as discussed in Section 3.3. Finally, activation with urea alone resulted in a degree of graphitization comparable to that of non-activated samples, confirming the role of KOH activation in preventing the stacking of (002) planes.

3.1.2. Bulk and surface composition

The morphology and composition of the synthesized materials were investigated by FESEM and EDX.

FESEM images of all activated samples are reported in Fig. 2, revealing irregular morphology with particle sizes generally exceeding 100 μm. For CS-K6 and CS-K7 only (Fig. 2a,b) the outer particle surfaces exhibit abundant macropores, likely due to the removal of external potassium salt particles during washing. Indeed, such macropores are much less abundant in CS-K8, and are absent in all CS-KUX samples.

The elemental composition of all activated samples was measured by EDX analysis. Three different areas, each approximately 500 μm^2, were analysed for each sample, with the average values (At. %) reported in Table 1. For all activated samples, EDX analysis detected C, O, K, and trace amounts of S, which is attributed to the use of H_2SO_4 as a dehydrating agent in the CS precursor preparation. As expected, N was detected only in CS-KUX samples. The C:O ratio is expected to increase as the carbonization temperature rises. This trend is clearly observable

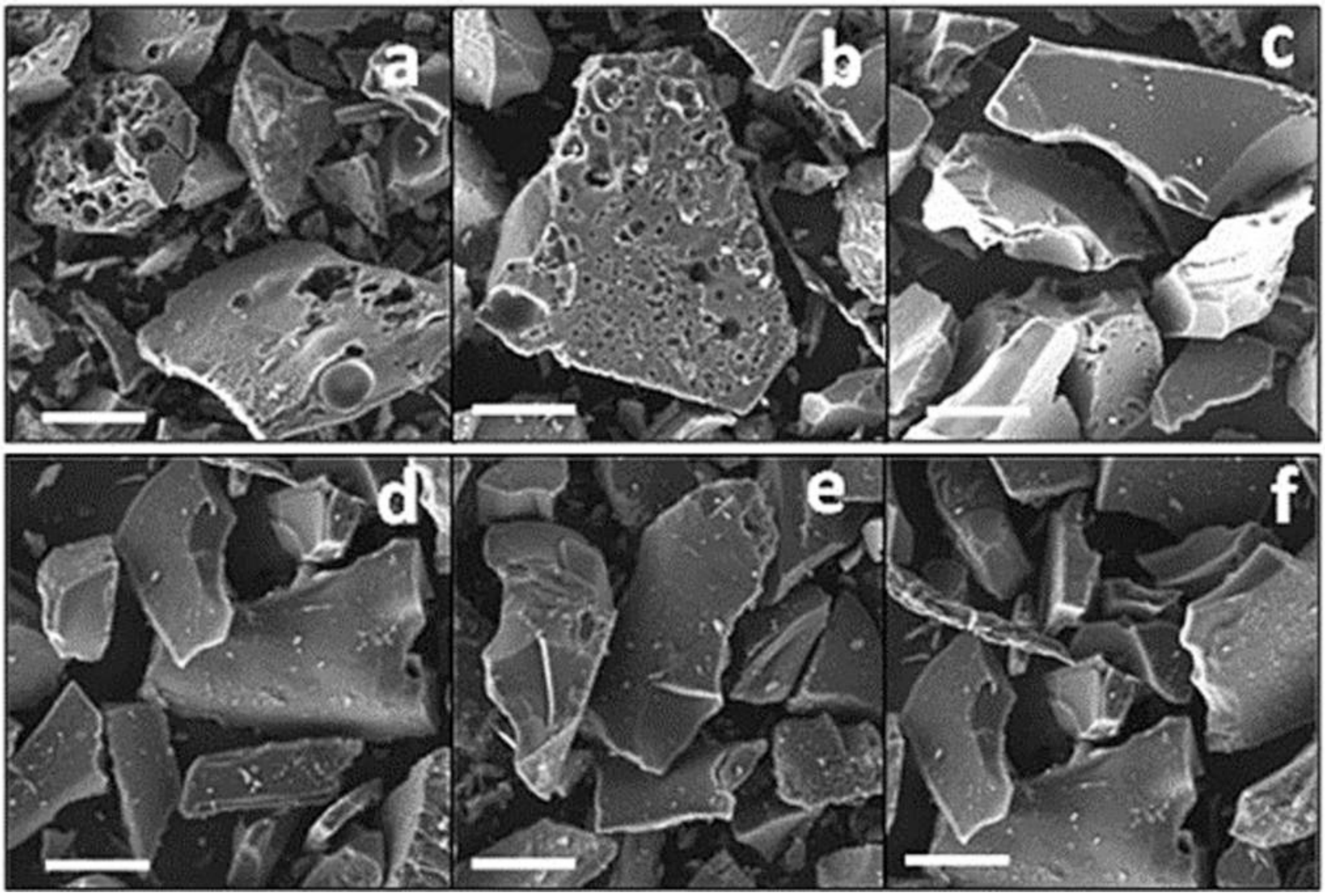

Fig. 2. FESEM images of CS-K6 (a), CS-K7 (b), CS-K8 (c), CS-KU6 (d), CS-KU7 (e), CS-KU8 (f). The scale bar corresponds to 100 μm.

in the CS-KU*X* samples, which do not contain oxygen-rich carbonate species. In agreement with the XRD results, the highest K contents were found in the CS-K6 and CS-K7 samples (Table 1). However, EDX maps (Fig. S3a) of selected carbon particles revealed a homogeneous distribution with no evident segregation of K-containing particles. These findings suggest that, in addition to segregating in the form of embedded (hydrogen)carbonate particles, potassium is finely dispersed in the carbon matrix in the form of intercalated potassium or surface K-complexes (*e.g.* C-O-K) [48]. K is also present in CS-KU*X* samples (Fig. S3b), and its content decreases with rising T_{act}. EDX maps of urea-activated samples also revealed a homogeneous distribution of K with no evident segregation.

Finally, a N content of 2.4, 3.1, and 7.1 at.% was measured for CS-KU8, CS-KU7, and CS-KU6 samples, respectively. A similar trend for these values was also measured by XPS analysis (Table 1, in brackets), confirming that N content decreases as T_{act} increases, and supporting an overall homogeneous distribution over bulk and surface for this element.

To integrate the morphological characterization with structural information at the nanoscale, a representative sample (CS-KU7) was analysed by HRTEM. The obtained images (Fig. 3a,b) confirmed the fully amorphous nature of the carbon matrix, already suggested by the complete absence of the (002) reflection in the XRD patterns. Small dark regions can be observed, originating from the partial re-deposition of the Pt protective layer during the lamella preparation process, when the material is cut by the thinning ion beam. Furthermore, the homogeneous distribution of N and K observed at low magnification in the FESEM-EDX analysis was further confirmed at the nanoscale (Fig. 3c–h, Pt was excluded from the quantitative analysis).

To gain insights into the nature of different N species, we measured N 1 s XPS spectra (reported in Fig. 4b). The spectra were fitted with three peaks, at binding energies of ≈ 398.2 ± 0.2 eV, 399.8 ± 0.1 eV, and 401.5 ± 0.2 eV: these components can be ascribed to pyridinic, pyrrolic/pyridonic, and quaternary N species, respectively [30,49–51]. We quantified the amounts of different N species in the samples (results reported in Fig. 4c). For sample CS-KU6, most of N is present as pyrrolic/pyridonic N (≈ 64 %), while pyridinic and quaternary N species account for ≈ 26 % and ≈ 10 %, respectively. Increasing the activation temperature from 600 °C to 700 °C and 800 °C led to a progressive decrease in the relative amount of pyrrolic/pyridonic N and an increase in the relative amount of pyridinic and quaternary N species. This conversion is due to the partial transformation of pyrrolic N into quaternary N at temperatures above 700 °C [52]. The large amount of pyrrolic and pyridinic N moieties in the CS-KU6 sample can contribute to the enhanced CO_2 capture performance of this sample, as both surface species were previously identified as active N-based functionalities for anchoring CO_2 molecules [53].

We also acquired high-resolution spectra in the regions of C 1 s and K 2p peaks (Fig. 4d) for all the CS-KU samples. The ratio between the intensities of K and C peaks decreases with increasing the T_{act} of the samples (Table S1), pointing toward lower K content in the samples prepared at higher T_{act}. These results are in line with the lower K contents detected by EDX in the samples activated at higher temperatures. The position of K $2p_{3/2}$ is similar for all the samples (292.8 ± 0.1 eV), indicating no substantial differences in K species across the samples. This binding energy value has been reported in the literature and attributed to R-O-K species [54]. The peak of C 1 s was fitted using six components [55], as reported in Fig. 4d and Table S1, to consider the different C species and relative allotropic forms. The shoulder at high binding energy, ascribed to C bound to carbonyl and carboxyl groups, is

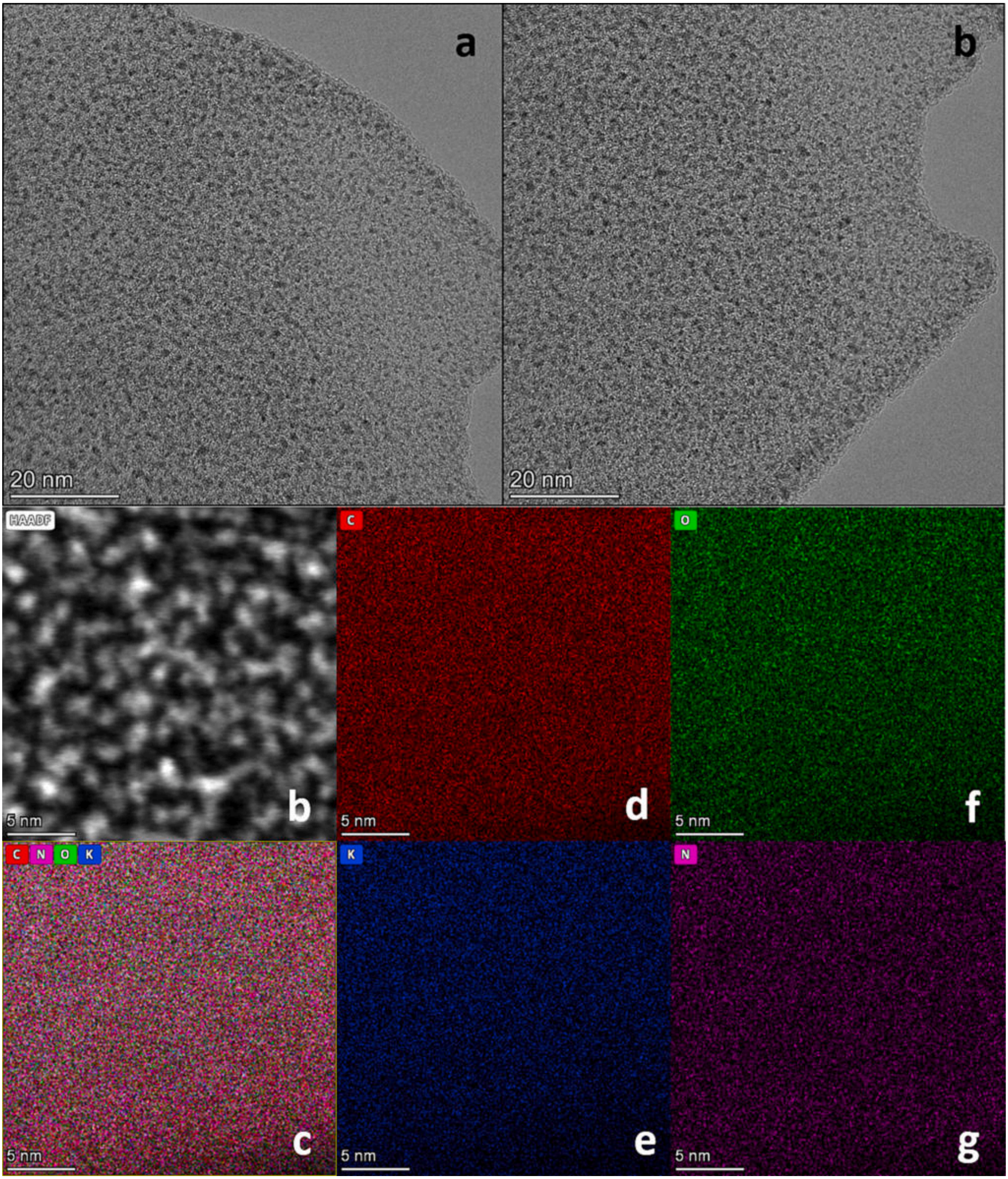

Fig. 3. HRTEM images (a,b) and EDX elemental mapping of CS-KU7.

more pronounced in the CS-KU 6 sample than in the other samples. This is consistent with the higher O content in the CS-KU6 sample. In the same region we can also detect bonds related to R-O-K and C-O-N.

3.1.3. TGA analysis

The inorganic residues (ash) remaining at the end of TGA (Fig. 5) can be associated with the total metal content in the samples. Indeed, a good correlation was observed between TGA residue and K content (as measured by EDX). The largest residues were found for CS-K6 and CS-K7

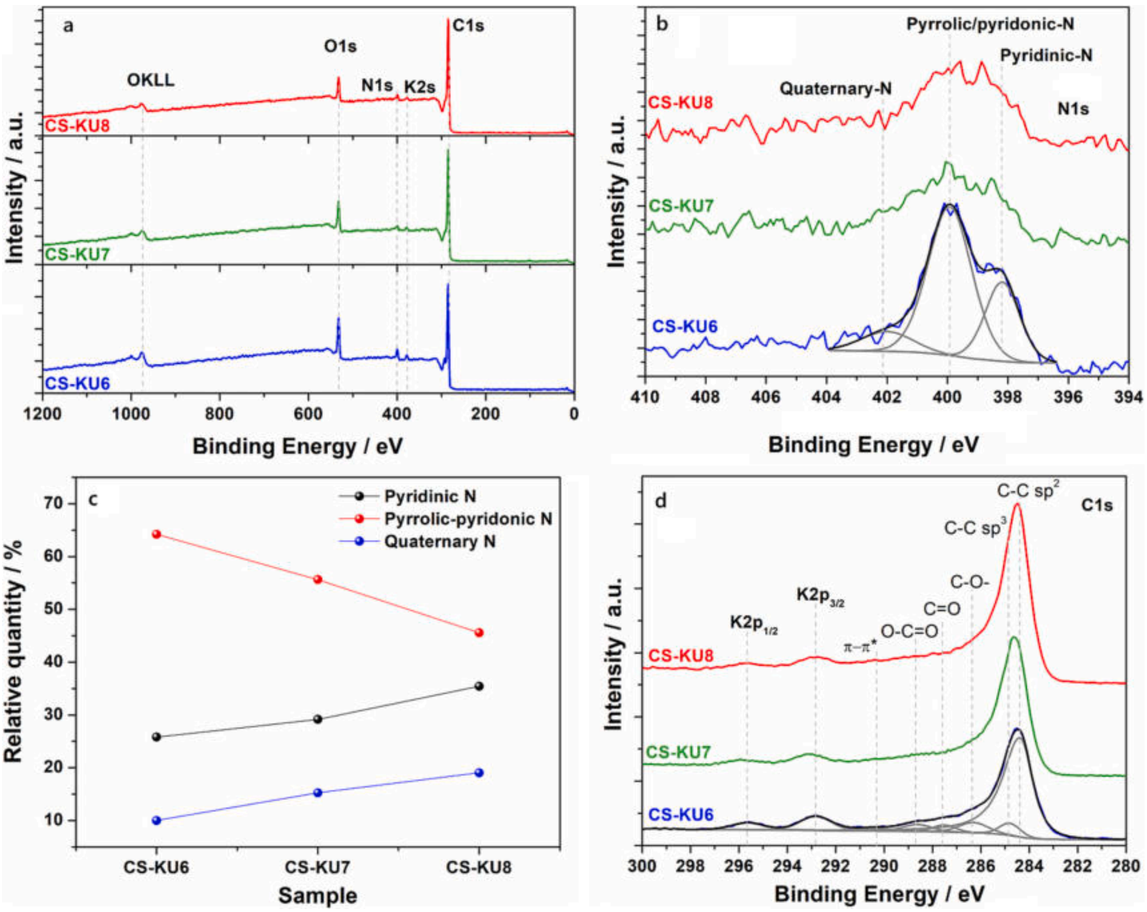

Fig. 4. XPS spectra for CS-KU6, CS-KU7 and CS-KU8: a) survey spectra; b) N1s HR region; c) N species relative quantity (%) according to the fitting procedure highlighted in (c) for sample CS-KU6; d) C1s and K2p HR regions.

(13.0 and 16.3 wt%, respectively), in line with EDX and XRD results showing the highest amount of K and the presence of K-containing phases in these samples. Likewise, for the KOH/urea-activated samples, higher residues were observed for $T_{act} \leq 700$ °C. Given the absence of crystalline K-containing phases, these samples exhibited lower residues (CS-KU6: 8.9 wt%; CS-KU7: 9.3 wt%) than the corresponding KOH-activated samples. Activation at $T = 800$ °C led to lower amounts of residue, regardless of the activating agent (3.5 and 4.7 wt% for CS-K8 and CS-KU8, respectively). For comparison, the TGA curves of CS-8 (non-activated) and CS-U8 (activated with urea only) are also reported in Fig. 5, showing residues below 1 wt%.

Analysis of the low-temperature region ($T < 150$ °C) of the TGA curves revealed a weight loss (approximately 7–11 wt%) for both CS-K*X* and CS-KU*X* samples prepared at $T_{act} \leq 700$ °C. For CS-K6 and CS-K7, the observed weight loss could be partly due to the decomposition of residual hydrogen carbonates evidenced by XRD. This explanation, however, cannot account for samples CS-KU6 and CS-KU7, which do not contain hydrogen carbonates. For these samples, the mass loss is more likely due to the desorption of H_2O and/or CO_2, pre-adsorbed upon air exposure onto specific strong adsorption sites. Indeed, the low-temperature weight loss is far less pronounced for CS-K8 and CS-KU8 samples, both characterized by a low K content, as well as for CS-K7-W (*i.e.* sample washed with HCl – Fig. S1b). This observation points to the presence of K species acting as adsorption sites, particularly abundant in samples activated at $T_{act} \leq 700$ °C. As observed by Liu et al. [25], these species are largely removed by HCl washing. In CS-KU*X* samples, the presence of N surface groups is also expected to enhance affinity for H_2O and CO_2 [56], thereby contributing to the observed low-temperature weight loss.

3.1.4. N_2 isotherms at −196 °CK

Fig. 6 reports N_2 isotherms at −196 °C of CS-K*X* (Fig. 6a) and CS-KU*X* (Fig. 6b) samples, while the corresponding BET SSA and porous volumes are reported in Table 2. To better illustrate the effect of the activating agent and activation temperature on the textural properties of our samples, the SSA and $V_{MP(t\text{-}plot)}$ values are also summarized in Fig. 7.

The samples prepared without an activating agent (*i.e.* CS-X) showed relatively low SSA (< 300 m^2/g) and total porous volume (< 0.14 $cm^3\ g^{-1}$). However, such properties were likely underestimated by N_2 adsorption at −196 °C. Indeed, the corresponding isotherms (Fig. S4a) showed an open hysteresis loop, suggesting the occurrence of N_2 diffusion limitations within ultra-micropores (*i.e.* pore width < 0.7 nm). This phenomenon is common in non-activated microporous carbons [57] and hinders the application of any model (*e.g.* NLDFT) to N_2 isotherms for determining micropore size distributions.

In contrast, the isotherms of KOH-activated samples (Fig. 6a) show H4-type hysteresis loops, more pronounced at $T_{act} = 800$ °C. The loop closes around the P/P_0 value (~0.4) associated with cavitation-controlled evaporation, suggesting the presence of wide mesopores connected to the external surface *via* narrow constrictions (<3–4 nm) [58,59]. CS-K8 exhibited much higher SSA and porous volume compared with the other CS-K*X* samples. These results are consistent with the absence of K-containing salts in sample CS-K8 and confirm that KOH becomes an effective activating agent only for $T_{act} \geq 800$ °C, when reactions (3), (4), and (5) occur. Notably, activation at 800 °C with K/C ratio > 1.0 (*i.e.* 1.5 for sample CS-K8–1.5) led to larger SSA (1851 m^2g^{-1}) and $V_{MP(t\text{-}plot)}$ (0.62 cm^3g^{-1}) compared with CS-K8 (1300 m^2g^{-1} and 0.39 $cm^3\ g^{-1}$). Nevertheless, this additional porosity does not enhance CO_2 uptake, suggesting that a K/C ratio of 1 is optimal for

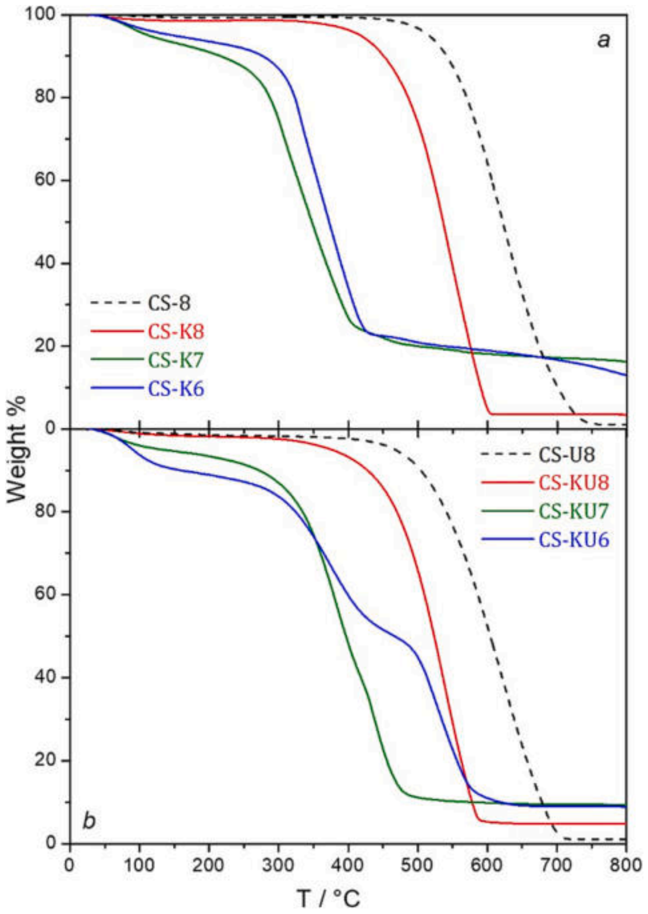

Fig. 5. TGA curves of CS-KX (a) and CS-KUX (b). For comparison, samples prepared without KOH are also reported as dotted lines (CS-8 in section a, and CS-U8 on section b).

subsequent co-activation with urea.

When urea is used as a co-activating agent, the materials displayed pure type-I isotherms with no hysteresis loops (Fig. 6b). As T_{act} increases, the isotherm knees at low P/P^0 gradually become more rounded, indicating broader pore size distributions. Compared with materials activated without urea, all CS-KU*X* samples exhibit higher SSA and porous volume, regardless of T_{act}. The addition of urea as an activating agent is particularly effective at low T_{act} (600 °C), leading to a threefold increase in SSA and V_{MP} compared with the CS-K6 sample.

The micropore size distribution of the activated samples and the corresponding cumulative pore volume curves were analysed using the NLDFT model applied to N_2 isotherms (Fig. 8). The microporous volumes $V_{MP(NLDFT)}$, obtained from the cumulative curves at 2 nm, are in good agreement with the values derived from t-plot analysis ($V_{MP(t\text{-}plot)}$), and are also reported in Table 2.

All CS-K*X* samples exhibit microporosity consisting exclusively of pores smaller than 1 nm. The microporous volume of CS-K8 is approximately twice that of CS-K7 and CS-K6. For comparison, Fig. 8 also includes the cumulative pore volume curve of CS-K8–1.5, which displays a broader micropore size distribution and a significantly higher microporous volume. For CS-KU*X* samples, the micropore size distribution is broader, especially for $T_{act} \geq 700$ °C. The curve of CS-KU8 crosses that of CS-KU7 and CS-KU6 at approximately 0.8 nm, suggesting a larger fraction of ultra-micropores in the latter two samples.

This observation can be related to the higher burn-off value observed for CS-KU8 (60 %) compared to CS-KU6 (20 %) and CS-KU7 (34 %). Actually, at $T_{act} = 800$ °C, the decomposition of K_2CO_3 leads to the release of CO_2, which may further react with carbon *via* gasification reactions. This additional activation step can contribute to the widening of micropores, thereby reducing the relative fraction of ultra-micropores in CS-KU8.

Table 2
Porous properties of the prepared samples determined from N_2 isotherms at −196 °C.

Sample	SSA / m^{2}g^{-1}	V_{TOT} / cm^{3}g^{-1}	$V_{MP(t\text{-}plot)}$ / cm^{3}g^{-1}	$V_{MP(NLDFT)}$ / cm^{3}g^{-1}
CS-6	187	0.10	0.10	n.a.
CS-7	298	0.14	0.14	n.a
CS-8	248	0.12	0.12	n.a
CS-K6	542	0.43	0.17	0.18
CS-K7	690	0.52	0.23	0.22
CS-K8	1300	0.89	0.41	0.39
CS-K8–1.5	1851	0.95	0.62	0.70
CS-KU6	1667	0.70	0.59	0.62
CS-KU7	2434	1.08	0.9	0.96
CS-KU8	2804	1.25	1.07	1.12
CS-U8	36	0.02	n.a.	n.a
CS-KCU6	1251	0.52	0.44	0.47
CS-KCU7	1895	0.83	0.68	0.74

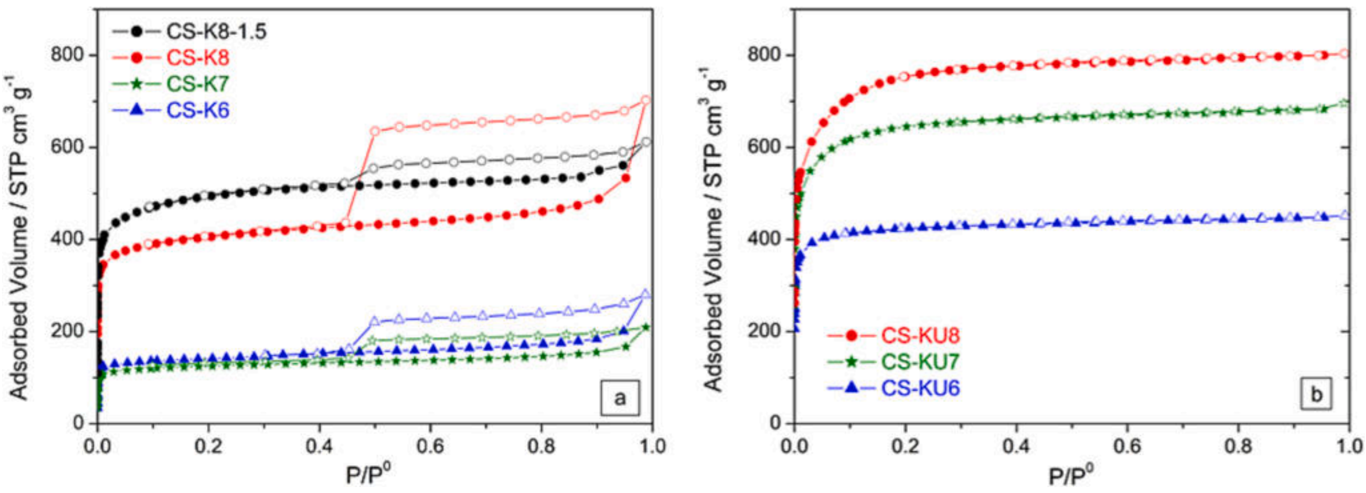

Fig. 6. N_2 isotherms at −196 °C for CS-KX (a) and CS-KUX (b) samples. Full and empty symbols refer to the adsorption and desorption branches, respectively.

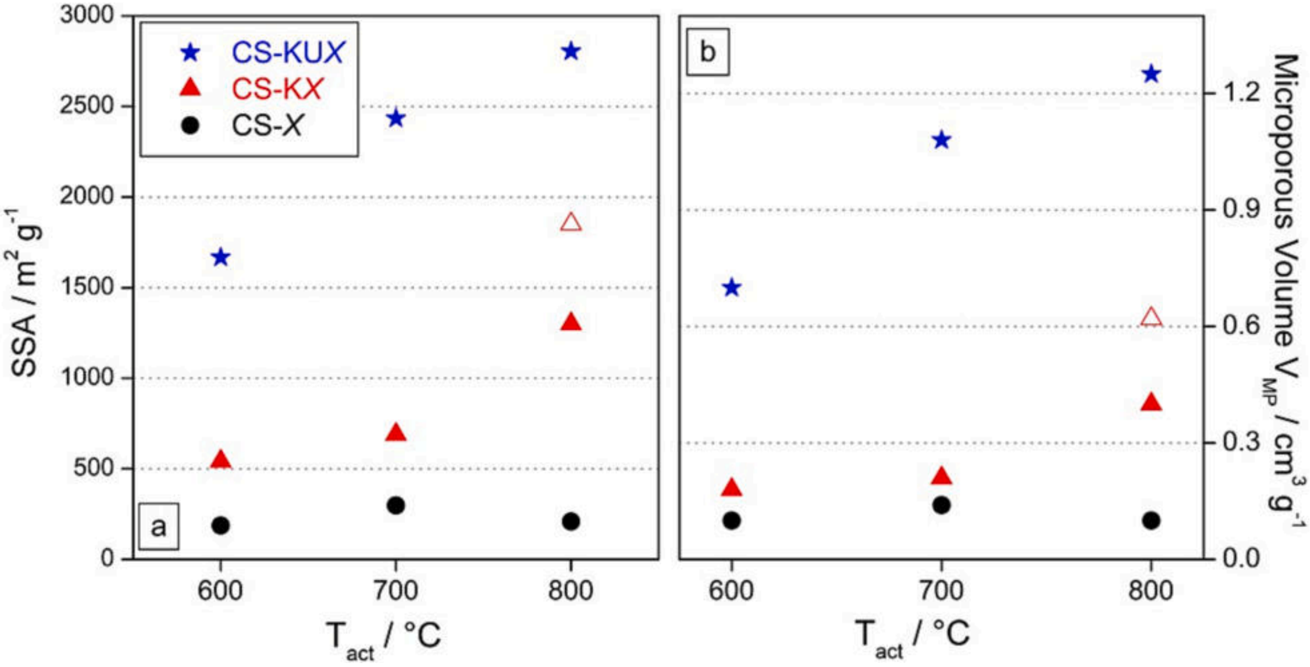

Fig. 7. SSA (a) and $V_{MP(t\text{-}plot)}$ (b) of CS-X (circles), CS-KX (triangles), and CS-KUX (stars) for different activation temperatures. Empty triangle refers to sample CS-K8–1.5 prepared with higher K/C ratio.

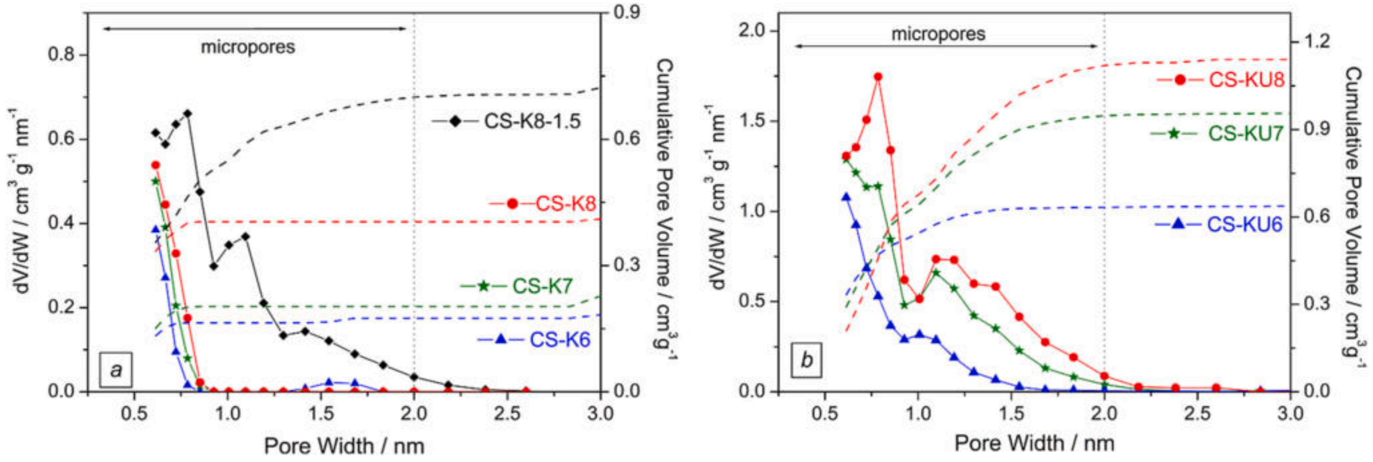

Fig. 8. Pore size distribution (PSD, solid lines with symbols, left y-axis) and corresponding cumulative pore volume curves (dashed lines, right y-axis) of CS-KX (a) and CS-KUX samples (b), obtained by applying the NLDFT method applied to N₂ isotherms. The micropores region (< 2 nm) is highlighted.

3.2. CO_2 adsorption properties

3.2.1. CO_2 adsorption isotherms

The CO₂ adsorption performance of the activated carbon materials was examined at 0 °C, 10 °C, and 20 °C, as shown in Figs. 9 and S5, with the detailed results presented in Table 3. Comparing the three sets of samples, the beneficial effect of the activation process is evident, leading to substantially different uptake capacities at both 0 °C and 20 °C. The values obtained at the maximum CO₂ pressure (*i.e.* 740 Torr) at 0 °C are summarized in Table 2 and Fig. S6a, falling in the 2.8–3.5 mmol g^{-1} range for CS-*X* samples, 3.7–4.5 mmol g^{-1} for CS-KX samples, and 6.7–7.5 mmol g^{-1} for CS-KUX samples. The latter clearly exhibited higher adsorption capacities than their counterparts prepared using KOH alone.

The highest uptake, 7.36 mmol g^{-1} (323.9 mg g^{-1}), was recorded for CS-KU7, surpassing all CS-KX samples and highlighting the beneficial role of urea in the activation mixture. By contrast, urea alone is not an effective activating agent. In fact, sample CS-U8 adsorbed only 2.90 mmol g^{-1}, similar to the non-activated CS-X carbons.

For CS-K*X* samples, the CO₂ uptake increases with T_{act}. This trend can be readily explained by the XRD patterns and N₂ isotherms, which indicate that an activation temperature above $T_{boil(K)}$ is needed to prevent the presence of residual K-based compounds that reduce porosity.

In contrast, the CS-KUX series shows similar capacities for T_{act} = 600 °C and 700 °C, followed by a drop at 800 °C. A preliminary, though not exhaustive, explanation for this behaviour comes again from N₂ isotherms, which revealed a larger fraction of ultra-micropores in CS-KU6 and CS-KU7. However, in addition to the micropore size distribution, the presence of specific adsorption sites could also contribute to enhancing the adsorption behaviour.

To assess the dynamic adsorption behaviour under conditions relevant to post-combustion CO₂ capture, breakthrough experiments were carried out on the most promising samples (*i.e.* CS-KUX) using a gas mixture containing 20 % CO₂ in N₂. The breakthrough curves shown in

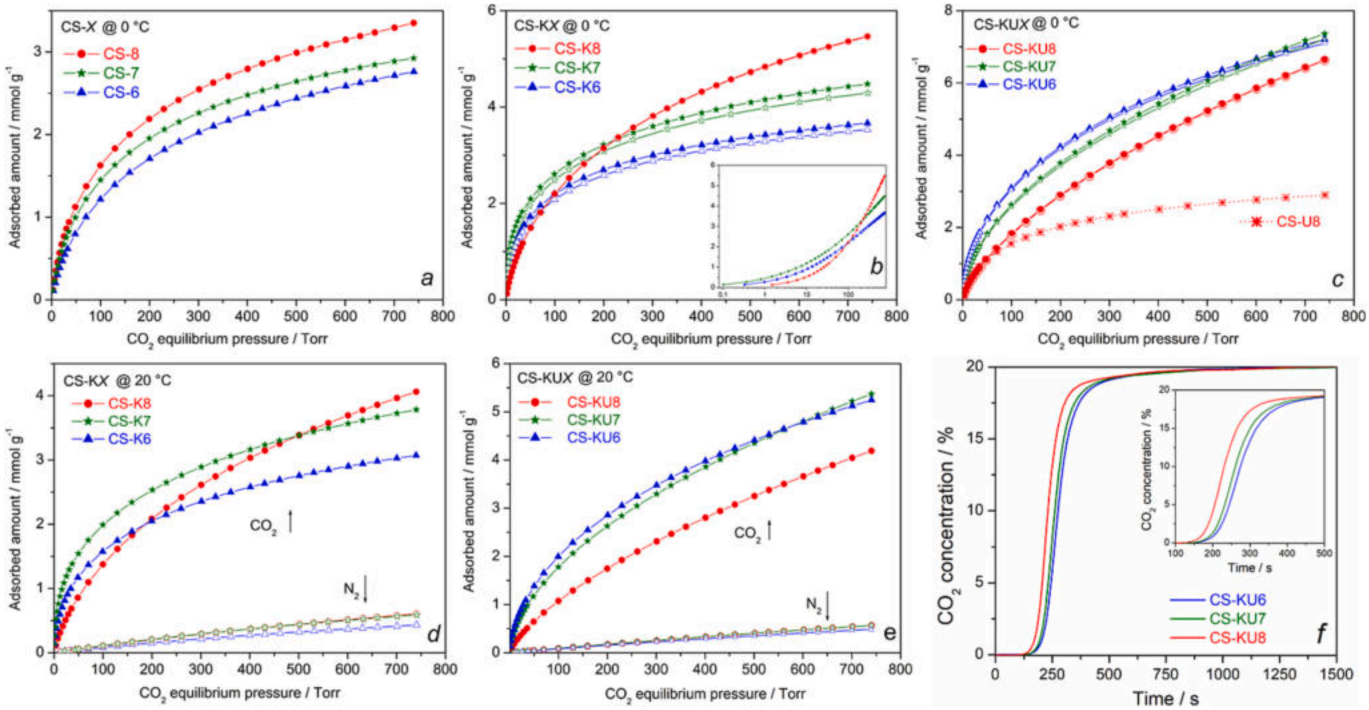

Fig. 9. CO_2 adsorption isotherms at 0 °C for CS-X (a), CS-KX (b) CS-KUX (c) samples. Empty symbols refer to second-run experiments. The inset of (b) shows a semi-logarithmic plot to highlight the low-pressure region where the isotherms intersect. Control experiment (CS-U8) is also reported in (c). CO_2 (full symbols) and N_2 (empty symbols) adsorption isotherms at 20 °C of CS-KX (d) and CS-KUX (e) samples. Breakthrough curves for 20:80 CO_2/N_2 at 30 °C and 760 Torr over CS-KUX samples (f).

Table 3
Summary of the parameters obtained from CO_2 adsorption isotherms.

Sample	$V_{MP(D-R)}$ cm^3 g^{-1}	$E_{0(D-R)}$ kJ mol^{-1}	Irrev. ads. mmol g^{-1}	CO_2 uptake @ 740 Torr mmol g^{-1}		Q_{st} kJ mol^{-1}
				@ 0 °C	@ 20 °C	
CS-6	0.17	31.5	n.a.	2.76	n.a.	n.a.
CS-7	0.18	32.6	n.a.	2.92	n.a.	n.a.
CS-8	0.21	32.3	n.a.	3.35	2.69	29–26
CS-K6	0.19	38.7	0.14	3.67	3.07	36–27
CS-K7	0.19	42.7	0.19	4.48	3.78	34–24
CS-K7-W	0.24	32.5	0.13	4.03	3.22	27–23
CS-K8	0.30	31.2	0.00	5.47	4.06	32–25
CS-K8–1.5	0.27	29.2	0.00	4.65	3.23	30–25
CS-KU6	0.29	35.8	0.10	7.20	5.24	38–28
CS-KU7	0.25	34.9	0.11	7.36	5.37	36–24
CS-KU8	0.25	30.5	0.00	6.64	4.19	30–25
CS-U8	0.19	34.5	n.a.	2.90	2.33	33–29

Fig. 9f exhibit a similar profile across all samples, suggesting comparable adsorption kinetics. Integration of the curves yielded dynamic CO_2 uptakes of 1.64, 1.48, and 1.04 mmol g^{-1} for samples CS-KU6, CS-KU7, and CS-KU8, respectively. The highest value observed for CS-KU6 is consistent with the superior uptake exhibited by this sample in the single-component CO_2 isotherms at corresponding partial pressures (*ca.* 150 Torr).

The excellent CO_2 adsorption performance of CS-KU7 and CS-KU6 is comparable to the best recent results reported in the literature (Table S2) and, combined with their ease of preparation, makes them promising candidates for industrial applications. In this regard, investigating the reversibility of the adsorption process is also essential. Therefore, for CS-K*X* and CS-KU*X* samples, two consecutive adsorption runs (at 0 °C) were performed, with an intermediate outgassing step at room temperature, to assess the presence of irreversibly adsorbed CO_2. The difference in CO_2 uptake between the two runs at the highest pressure corresponds to the amount of irreversibly adsorbed CO_2 and is reported in Table 2. A low irreversible fraction (< 5 % of the total adsorbed amount) was observed only for samples activated at 600 °C and 700 °C, being slightly higher for samples activated with KOH only, confirming that CO_2 physisorption is the dominant mechanism. Irreversibility is most probably due to very strong sites, associated with K- and/or N-based species, which are more abundant in samples activated at lower temperatures.

This hypothesis is supported by TGA (Fig. 5) and is further confirmed by both the characteristic energy E_0, obtained from the D-R plots of CO_2 isotherms, and the isosteric heats of CO_2 adsorption (Q_{st}) at low coverages (both reported in Table 3).

TGA curves for CS-K6, CS-K7, CS-KU6, and CS-KU7 samples (*i.e.* those exhibiting irreversibly adsorbed CO_2) showed a weight loss ranging from 7 to 11 wt% at $T < 200$ °C (with a maximum in DTGA curves at 65–85 °C), likely due to the desorption of CO_2 and/or moisture pre-adsorbed onto the samples during air exposure. The thermal treatment at 250 °C preceding the first adsorption run ensures the complete removal of these adspecies. Accordingly, the same samples exhibited the highest E_0 value (ranging from 35 to 42 kJ mol^{-1}) and Q_{st} at low coverage (34–38 kJ mol^{-1}), indicating the presence of strong adsorption sites with a high affinity for CO_2. The strongest fraction of these sites may interact with CO_2 in a way that remains irreversible at room temperature.

A minor contribution from residual K_2O (which could chemisorb CO_2, forming carbonates) cannot be excluded. Although XRD did not show peaks corresponding to this phase, it is possible that small amounts of K_2O, especially in the form of embedded or poorly crystalline nanoparticles, remained undetected. This hypothesis may be particularly relevant for CS-K6 and CS-K7 samples, which also showed the presence of bicarbonate species, possibly formed *via* surface reaction of atmospheric CO_2 with residual basic sites. Nevertheless, some residual K_2O in these samples may not have reacted under ambient conditions and could potentially become reactive in the presence of elevated CO_2 partial pressures, such as those applied during adsorption measurements. We therefore do not exclude that residual K_2O could play a minor role in the observed irreversibility.

The reversibility of adsorption and the cyclic stability were further assessed by an extended cyclic adsorption–desorption test consisting of nine cycles at 20 °C, performed on the best-performing sample (CS-KU7), as shown in Fig. 10. The first eight adsorption runs were followed by outgassing under vacuum at room temperature (30 min, 20 °C), while the last cycle was preceded by outgassing at a slightly higher temperature (30 min, 60 °C). After five consecutive adsorption–desorption cycles, the CO_2 uptake stabilized at approximately 96 % of the initial value, indicating excellent stability and reusability. Moreover, mild regeneration at 60 °C prior to the final cycle effectively restored the CO_2 uptake to a value comparable to the initial one. These findings confirm that the decrease in CO_2 uptake observed during the first eight cycles originates from a limited number of very strong adsorption sites, from which CO_2 is released after gentle heating to 60 °C. This high level of cyclic stability indicates that the material is well-suited for industrial use, providing consistent and long-lasting CO_2 capture with minimal performance loss over time, although mechanical strength under Pressure-Swing Adsorption (PSA) conditions still needs to be evaluated.

The characteristic energy E_0 and the microporous volume ($V_{MP(D\text{-}R)}$) were obtained by applying the Dubinin–Radushkevich (D-R) method to CO_2 adsorption isotherms, and the corresponding D-R plots are shown in Fig. 11.

For all CS-*X* samples (Fig. 11a–c), $V_{MP(D\text{-}R)}$ is larger than the total pore volume obtained from N_2 isotherms, clearly indicating the presence of ultra-micropores that are not accessible to N_2 at −196 °C. Such behaviour is typical of carbonized materials with low burn-off, which exhibit a micropore volume measured from CO_2 isotherms exceeding that obtained from N_2 isotherms [60]. Indeed, compared to N_2 at −196 °C, CO_2 at 0 °C has a smaller kinetic diameter and larger kinetic energy, enabling it to overcome the diffusional constraints imposed by narrower micropores. Very similar E_0 values were obtained for CS-*X*, ranging from 31 to 32 kJ mol^{-1}, suggesting that their different CO_2 adsorption behaviour is mainly due to the different $V_{MP(DR)}$. The characteristic energy E_0 is often related to the pore width: the larger the former, the smaller the latter. Stoeckli et al. proposed an equation (Eq. (10)) to calculate the pore width (L) of porous carbons with characteristic energy in the range of 20 to 40 kJ mol^{-1} [61].

$$L(\mathrm{nm}) = 10.8/(E_O - 11.4) \tag{10}$$

According to Eq. (10), pore width in the 0.51–0.54 nm range are obtained for CS-*X* samples. Notably, these dimensions lie well below the starting point of the cumulative pore volume curve derived from N_2 isotherms.

The D-R plots of CS-*X* are quite linear across the entire range of pressures, suggesting a homogeneous pore distribution. The downward deviation at very low pressure (high P^0/P) is a consequence of the narrow size of the micropores, which may result in diffusional or steric limitations even for CO_2 adsorption [62]. As expected, such limitations are not observed for CS-K*X* (Fig. 11d–f) and CS-KU*X* (Fig. 11g–i) samples, where a well-developed porous structure is provided by chemical activation.

For CS-K*X* samples, the experimental data are fitted by D-R equation across almost the entire pressure range, with only a limited upward deviation from linearity at high pressures (low P^0/P). This feature agrees with N_2 adsorption results, which revealed homogeneous microporosity consisting entirely of pores smaller than 1 nm for all CS-KX samples (Fig. 8a). The trend of $V_{MP(D\text{-}R)}$ as T_{act} increases is also similar to that of

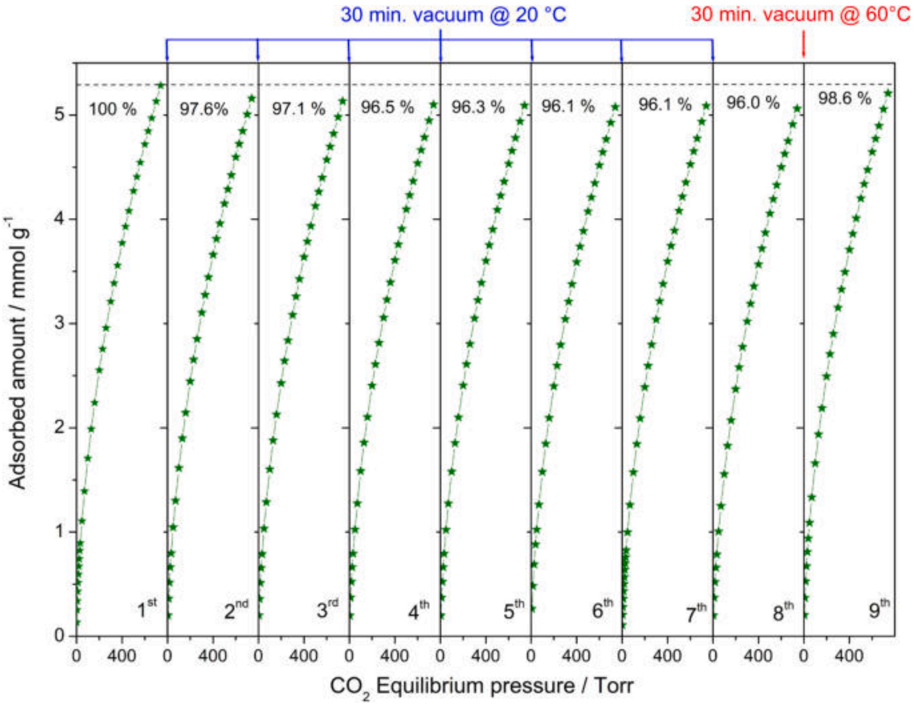

Fig. 10. CO_2 adsorption isotherms at 20 °C for the CS-KU7 sample over multiple consecutive cycles under vacuum regeneration conditions.

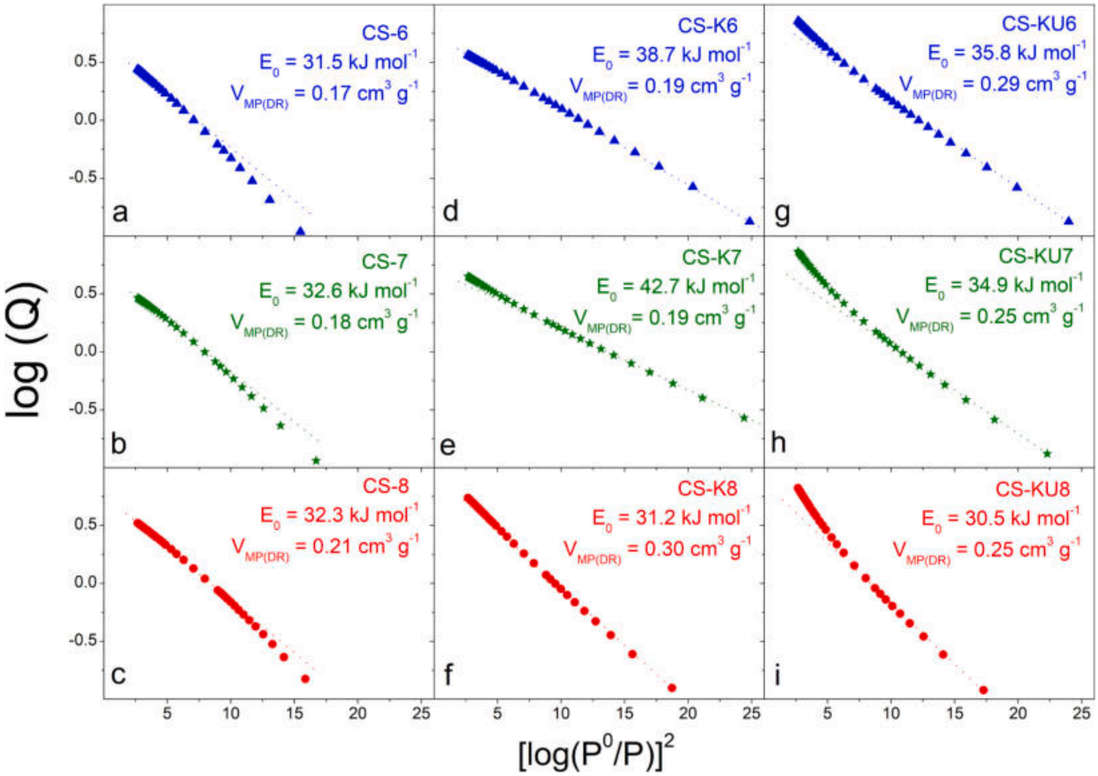

Fig. 11. D-R plots for CS-*X* (a), CS-K*X* (b), and CS-KU*X* (c) obtained from CO_2 isotherms at 0 °C.

$V_{MP(NLDFT)}$, with the highest value found for CS-K8. On the other hand, samples CS-K6 and CS-K7 showed higher values of E_0 (*ca.* 39 and 42 kJ mol^{-1}, respectively, compared to 31 kJ mol^{-1} for CS-K8), in line with their different isotherm shape. In fact, the CO_2 isotherm of CS-K8 shows a less defined knee, and lies below those of CS-K6 and CS-K7 for pressure lower than *ca.* 100 Torr (see inset of Fig. 9b). Applying Eq. (10) to CS-K6 and CS-K7 samples may yield misleading results, returning very small L values of 0.39 and 0.36 nm, respectively. In principle, such small pores (only slightly larger than the kinetic diameter of CO_2) should lead to diffusion limitations similar to those observed for the CS-*X* samples, which exhibited negative deviations in the D-R plots. We thus attribute the high E_0 values of these samples not solely to reduced pore size but also to the presence of K-based adsorption sites with high polarizing power. These sites, similar to those observed in cation-exchanged zeolites [46], enhance the interaction between CO_2 molecules and the carbon surface.

As for CS-K*X* samples, it is also worth comparing the adsorption capacities and porous properties of CS-K8 and CS-K8–1.5, both activated under the same conditions (*i.e.* KOH alone, $T_{act} = 800$ °C) and showing similar (and low) K content. As stated above, increasing the K/C ratio from 1.0 to 1.5 led to a decrease in CO_2 uptake at both 0 °C and 20 °C (Fig. S7a). This result was not predictable based only on the corresponding N_2 cumulative pore volume curves (Fig. 7a), which start from nearly the same point (*i.e.* ~ 0.33 cm^3 g^{-1} at 0.6 nm), and indicate a larger and more heterogeneous microporous volume for CS-K8–1.5. This heterogeneity was further confirmed by the D-R plot of CS-K8–1.5, showing a marked upward deviation (Fig. S7b). More importantly, D-R analysis yielded a lower $V_{MP(D\text{-}R)}$ (0.27 *vs* 0.30 cm^3 g^{-1}) for CS-K8–1.5, underscoring key differences in the ultra-micropore fraction that account for its inferior adsorption performance.

For CS-KUX samples, D-R plots exhibit a strong upward deviation from linearity at high pressure (low P^0/P), indicating significant heterogeneity in the adsorption sites. Consequently, experimental data for $[\log(p^0/p)]^2 < 7.0$ (corresponding to an absolute pressure > of ~ 70 Torr) were excluded from curve fitting. Thus, the obtained E_0 and $V_{MP(D\text{-}R)}$ values reported in Table 2 refer only to the stronger fraction of adsorbed CO_2. Similar to the CS-K*X* samples, higher E_0 values were obtained for $T_{act} \leq 700°$ (*i.e.* 35–36 kJ mol^{-1}); however, in this case, the highest $V_{MP(D\text{-}R)}$ was obtained at 600 °C. The high E_0 values for CS-KU6 and CS-KU7 likely stem from their narrow microporosity coupled with K- and N-based adsorption sites with high CO_2 affinity.

Overall, the present results clearly demonstrate that CO_2 adsorption at low pressure (< 100 Torr) is strongly influenced by both high E_0 and $V_{MP(D\text{-}R)}$, whereas the presence of super-micropores enhances adsorption at higher equilibrium pressure (up to ambient pressure). The outstanding CO_2 adsorption performance of CS-KU6 and CS-KU7 can be attributed to the synergistic effect of three key factors: *i)* a large $V_{MP(D\text{-}R)}$ associated with the presence of ultra-microporosity, *ii)* the presence of specific adsorption sites with strong affinity for CO_2, enhancing the interaction energy, *iii)* the presence of wider micropores adsorbing CO_2 at higher pressure. This latter feature may also be beneficial for practical applications, as it ensures the pathways for CO_2 diffusion into the ultra-micropores.

In line with these observations, no clear correlation is expected between the maximum adsorption uptake and any individual porous property. When plotting CO_2 uptake against SSA, $V_{MP(t\text{-}plot)}$ or $V_{MP(D\text{-}R)}$, a significant data dispersion is obtained (Fig. S6b-d). Although an increase in SSA and $V_{MP(t\text{-}plot)}$ enhances performance, the absence of a linear regression through the origin confirms that N_2 adsorption at −196 °C underestimates a significant fraction of the pore/surface area active in CO_2 adsorption. On the other hand, despite the considerable scatter, a rough linear regression through the origin is obtained for $V_{MP(D\text{-}R)}$ ($R^2 = 0.8283$). The weak correlations observed in Fig. S6 further confirm that CO_2 adsorption in our materials is not solely governed by micropore size distribution but is also strongly influenced by the presence of specific high-affinity adsorption sites.

3.2.2. *Isosteric heat of adsorption and IAST selectivity*

To further investigate the strength of CO_2 interaction with our sorbents, isosteric heat of adsorption (Q_{st}, as shown in Fig. 12a,b) was

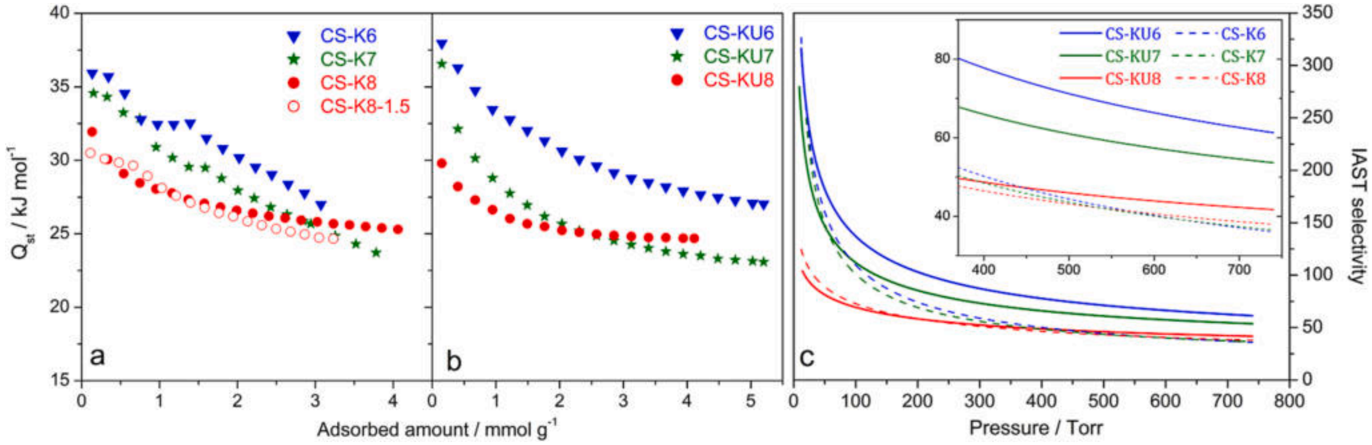

Fig. 12. Isosteric heat of adsorption Q$_{st}$ of CS-KX (a) and CS-KUX (b); IAST selectivity at 20 °C for mixture with 0.15/0.85 CO_2/N_2 molar composition (c); inset of section c shows enlargement of the near-ambient pressure region.

calculated by applying the Clausius-Clapeyron equation to the CO_2 adsorption isotherms at 0 °C and 20 °C. The upper coverage limit shown in Fig. 12a,b correspond to the maximum uptake measured at 20 °C. In general, a high Q$_{st}$ value (> 30–35 kJ mol^{-1}) is desirable for applications requiring high CO_2 uptake at very low pressures (*e.g.* flue gas separation). When Qst exceeds ~50 kJ mol^{-1}, however, sorbent regeneration *via* PSA becomes challenging [63]. The Q$_{st}$ values at both maximum and minimum coverages for our sorbents are also summarized in Table 2. The trend in Q$_{st}$ at low coverage is in good agreement with that of characteristic energy E$_0$: samples activated at $T \leq 700$ °C exhibit stronger interactions, with initial Qst values of 38–35 kJ mol^{-1}, whereas those activated at 800 °C fall in the 30–32 kJ mol^{-1} range. Discrepancies between the energies derived from the D–R model and the Clausius-–Clapeyron equation are reported in the literature [10,30], and may be primarily due to the β value used in D-R equation. Furthermore, D-R model is based on the potential theory of Polanyi, assuming that the adsorption mechanism is dominated by micropore filling rather than surface coverage [42]. The presence of strong specific adsorption sites could make this assumption not fully justified. Indeed, early criticism of Polanyi's model stressed that it neglects electrical interactions between the gas and the surface.

The isosteric heat of adsorption also reflects surface heterogeneity. For an ideal homogeneous adsorbent, Q$_{st}$ is constant with coverage, whereas on heterogeneous surfaces it decreases as progressively weaker sites are occupied. Among all activate samples, CS-K8 and CS-KU8 exhibited less heterogeneous surfaces. After an initial decrease, their Q$_{st}$ reaches an almost constant value (around 25 kJ mol^{-1} for adsorbed amounts greater than *ca.* 1.5 mmol g^{-1}), which is close to the upper limit of the reported Q$_{st}$ for common carbon-based adsorbents [64]. In contrast, the variation of Q$_{st}$ with coverage is much more pronounced for samples activated at T$_{act}$ ≤ 700 °C, indicating more heterogeneous interactions. Heterogeneity in our materials arises from both the micropore-size distribution and surface heteroatoms, specifically K and N. However, discerning the individual influence of each factor on Q$_{st}$ is not straightforward. In this regard, some insights into the role of K-based sites are provided by comparing CS-K7 and its acid-washed analogue CS-K7-W (Fig. S7e). At low coverage, Q$_{st}$ for CS-K7-W drops from 27 to 23 kJ mol^{-1}, whereas CS-K7 falls from 35 to 23 kJ mol^{-1}.. Interestingly, theoretical calculations [65] suggested that the introduction of K-based polar groups induces local polarization and charge separation in carbon, thus facilitating CO_2 adsorption through electrostatic interaction. The calculated adsorption energy of approximately 36 kJ mol^{-1} is consistent with our data for K-containing samples. Notably, HCl washing led to an increase in V$_{MP(D-R)}$ (Fig. S7d) but resulted in a decrease in the CO_2 uptake. These observations suggest that, in addition to strengthen adsorbate-adsorbent interactions, the presence of strong specific sites could increase the uptake efficiency of micropores by increasing the density of the adsorbed phase. For CS-KU*X* samples, such sites include both K and N-based centres. In particular, CS-KU6 showed the highest amount of pyrrolic surface groups, which are considered beneficial for CO_2 uptake [5,39,66,67]. Accordingly, this sample showed the highest Q$_{st}$ over the entire coverage range. In this regard, the comparison between CS-KU6 and CS-K8.15 is particularly illustrative. These two samples exhibit very similar textural properties, with comparable BET surface area (1851 and 1667 m^2/g), D-R micropore volume (0.27 and 0.29 cm^3 g^{-1}), and PSD (Fig. S8). Despite this, CS-KU6 displays both a significantly higher CO_2 uptake and consistently higher Q$_{st}$ values across the entire coverage range. This result clearly highlights the role of K- and N-based surface sites in enhancing CO_2 adsorption properties, beyond what can be explained by surface area and porosity alone. We hypothesize that the improved performance (in terms of both Q$_{st}$ and CO_2 uptake) introduced by the polarizing sites could also be due to a better exploitation of the supermicropores. In this regard, theoretical studies [3] showed that in pure carbon slit pores ≥0.8 nm (at 0 °C and sub-atmospheric pressures) CO_2 forms two monolayers on the opposite pore walls, with the CO_2 molecules adsorbing parallel to the walls and leaving the central part of the pores unfilled. The presence of polarizing centres may facilitate the formation of linear adducts perpendicular to the pore walls similar to those observed in cation-exchanged zeolites [46], and/or enhance adsorbate-adsorbate interaction through polarization effects, leading to a more effective utilization of the supermicropores. Interestingly, very recent theoretical results demonstrate that when the pore size exceeds 0.6 nm, K doping significantly increases the CO_2 adsorption uptake [28]. Ongoing studies will employ *in-situ* spectroscopy to clarify the nature of these specific interactions. On the other hand, the presence of K- and N-based functionalities is expected to increase the hydrophilicity of the samples [1,56], making the sorbents suitable for dry flue gas conditions. In addition to moisture, the potential effect of acidic gases on adsorption performance remains an important aspect for future investigation under real flue gas conditions.

For practical applications, selectivity over N_2 is highly desirable. The Ideal Adsorption Solution Theory [45] is a simple and widely used technique [5,30,65,66,68,69] for predicting CO_2/N_2 selectivity based on the single-component gas adsorption results. Thus, we measured N_2 adsorption isotherms at 20 °C (Fig. 9d,e) for our ACs and calculated the IAST selectivity for a 0.15/0.85 CO_2/N_2 molar mixture (Fig. 12c). At the total pressure of 740 Torr, the highest selectivity factor of 61 was calculated for CS-KU6, followed by CS-KU7 (54) and CS-KU8 (42). In contrast, samples activated with KOH alone exhibited lower selectivity at this pressure, regardless of T$_{act}$. Interestingly, the most selective materials also have the highest N-content, corroborating earlier reports that basic N functionalities enhance CO_2/N_2 selectivity [5,39,65,69,70].

3.3. Role of urea in the activation mechanism

Our results clearly indicate that, in addition to generating N-containing functional groups, urea plays a crucial role in the development of the porous network, as demonstrated by the comparison of SSA and pore volumes of samples prepared with and without urea. On the other hand, we found that urea is not an efficient activating agent on its own; rather, it acts synergistically with KOH, preventing the formation of residual potassium carbonates trapped within the carbon matrix. Notably, the burn-off measured for CS-K*X* (18 %, 29 %, and 60 % for X = 6, 7, and 8, respectively) and CS-KU*X* (20 %, 34 % and 60 % for X = 6, 7 and 8, respectively) samples was primarily dependent on T_{act} rather than the activating agent. Nevertheless, the samples activated with both KOH and urea exhibited significantly higher total pore volumes, despite having similar burn-off values. This indicates that, in the presence of urea, KOH is exploited much more efficiently in the generation of microporosity. The presence of macropores (which do not contribute to the total pore volume measured by N_2 adsorption), observed through FESEM only in the CS-KX samples, further supports this conclusion.

The use of KOH and urea as activating agents for the preparation of N-rich porous carbons is well-documented in the literature [10,11,30,35,36]. However, while the activation mechanism using only KOH has been extensively elucidated, the mechanism related to KOH/urea activation has not yet been thoroughly investigated [10,71,72]. In this context, valuable insights come from studies on the activation of N-enriched precursors [72,73]. Sevilla et al. examined the activation mechanism occurring in the preparation of nanoporous carbons from potassium citrate and urea [72]. Notably, they demonstrated that potassium carbonate (derived from citrate decomposition) reacts with urea at relatively low temperatures (*i.e.* 150 °C), forming potassium cyanate according to Eq. (11).

$$OC(NH_2)_2 + K_2CO_3 \rightarrow 2\ KOCN + 2\ NH_3 + H_2O + CO_2 \quad (11)$$

Potassium cyanate is then reduced to potassium cyanide by carbon, according to the reaction (Eq. (12)).

$$KOCN + C \rightarrow KCN + CO \quad (12)$$

The oxidation of carbon by potassium cyanate was identified as the primary mechanism for pore development at 650 °C. Notably, NH_3, CO_2, and H_2O produced in reaction (11) may also serve as physical activating agents [1], thereby further contributing to the formation of the porous network. Although our synthesis involves a one-step activation, where both urea and KOH are added simultaneously to the CS precursor, we believe that reactions (11) and (12) occur in our system already at 600 °C, leading to the consumption of potassium carbonate formed in reactions (1) and (2). Accordingly, the CS-KUX samples exhibited greater and more heterogeneous microporosity compared to the CS-KX samples (Fig. 8). This characteristic may also facilitate the removal of residual potassium salts during the washing phase. While the proposed formation of KOCN and $(NH_4)_2CO_3$ is supported by literature data, further experimental investigations will be conducted to clarify the activation mechanism.

These considerations suggest that, in the presence of urea, KOH could be replaced with the less corrosive K_2CO_3, thus making the synthesis more appealing from an industrial point of view. Given its decomposition temperature and the temperature at which it is reduced by the carbon matrix, potassium carbonate alone is generally employed at $T_{act} > 700$ °C [74]. Interestingly, we found that one-pot activation of CS precursor using a K_2CO_3/urea mixture at 600 (sample CS-KCU6) and 700 °C (sample CS-KCU7) yields porous carbons free of potassium (hydrogen)carbonate residues (as confirmed by XRD reported in Fig. S2a), with excellent CO_2 uptake at 0 °C of 6.87 and 7.81 mmol g^{-1}, respectively (Fig. 13). Notably, CS-KCU7 showed even better performance than its counterpart prepared with KOH and urea, demonstrating the high potential of this activation method. Further optimizations of CS activation with K_2CO_3 and urea, as well as thorough characterization of the resulting materials, is currently under investigation. Such studies pave the way for new insights into the design of high-performance adsorbents and open up promising possibilities for scalable applications in CO_2 capture and other environmental processes.

Although a detailed techno-economic analysis is beyond the scope of this study, a preliminary estimation based on current industrial prices of the raw materials (sucrose, KOH, urea, and H_2SO_4) suggests that the cost of raw materials for producing 1 ton of activated sample falls in the range of 2700–3400 \$ t^{-1}. This estimation does not include costs associated with equipment, energy consumption, or labour. While the use of

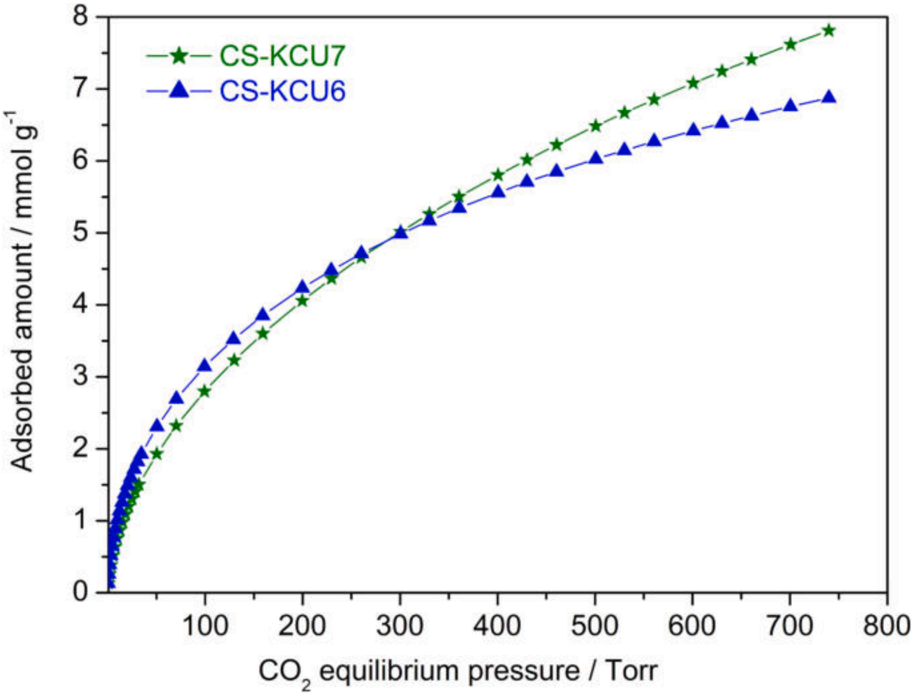

Fig. 13. CO_2 adsorption isotherms at 0 °C for samples prepared with K_2CO_3 and urea.

sucrose as a carbon precursor may result in higher raw material costs compared to biomass wastes, it offers a significant advantage in terms of process simplicity and energy efficiency, as it avoids the need for a pre-carbonization step typically required for biomass-derived materials.

4. Conclusion

In this study, sucrose-derived activated carbons (ACs) for CO_2 capture were successfully prepared through a one-step activation process. We showed the crucial role of activating agents (KOH or K_2CO_3 and urea) and activation temperature (600, 700 and 800 °C) in tailoring the textural and chemical properties of the resulting materials.

Using KOH alone as an activating agent, an optimal activation temperature (T_{act}) of 800 °C was required to achieve a well-developed porous structure free of residual potassium (hydrogen)carbonates, showing moderate CO_2 uptake (5.47 mmol g^{-1} at 0 °C and 740 Torr) and a heat of adsorption (25 kJ mol^{-1}) similar to that of common carbon-based adsorbents. Conversely, the samples obtained at lower T_{act} exhibited lower CO_2 uptake but higher heat of adsorption due to the presence of particularly strong adsorption sites originating from the intercalation of K in the carbon matrix. The role of these polarizing centres in enhancing the CO_2 heat of adsorption has often been overlooked in previous research, as they are effectively removed by the final HCl washing step commonly adopted in many synthesis procedures.

In the samples activated with KOH and urea, K was only present as intercalated K-species, pointing to a synergistic effect between KOH and urea in preventing the formation of (inactive) segregated K salts and in maximizing K utilization. Activation at moderate temperatures (600–700 °C) proved especially effective in balancing porosity development and surface functionalization, yielding materials with outstanding CO_2 uptake and selectivity. Specifically, the incorporation of both K and N surface species enhanced CO_2 affinity by increasing adsorption energy and selectivity, while preserving a microporous structure with high specific surface area. The sample activated at 700 °C using KOH/urea exhibited a CO_2 uptake of 7.36 mmol g^{-1} at 0 °C and 740 Torr. This exceptional performance resulted from the combination of a large fraction of ultra-micropores and the simultaneous functionalization with K sites and pyrrolic N moieties, which provided multiple CO_2 anchoring sites. Furthermore, the presence of K and N- based polarizing centres may also enhance the effective utilization of the super-micropores, optimizing them for CO_2 adsorption.

Finally, we showed that the tailored porosity and composition of the samples obtained through KOH/urea activation lead to higher CO_2/N_2 selectivity (up to 61 at 20 °C for a 15:85 CO_2:N_2 mixture) compared to those activated with KOH only, highlighting their potential as effective CO_2 sorbents in flue gas applications.

From an industrial perspective, replacing KOH with K_2CO_3 in the presence of urea emerges as a promising strategy for reducing synthesis costs and improving environmental compatibility. Overall, this work provides a deeper insight into the interactions governing CO_2 adsorption on ACs and offers a scalable approach for developing efficient sorbents for industrial applications.

CRediT authorship contribution statement

Marco Etzi: Writing – review & editing, Writing – original draft, Methodology, Investigation, Data curation, Conceptualization. **Enrico Sartoretti:** Investigation, Conceptualization. **Samir Bensaid:** Writing – original draft, Data curation, Conceptualization. **Marco Allione:** Writing – original draft, Investigation. **Sara Ferraris:** Writing – review & editing, Writing – original draft, Methodology, Investigation, Formal analysis, Data curation. **Micaela Castellino:** Writing – review & editing, Writing – original draft, Methodology, Investigation, Conceptualization. **Marco Armandi:** Writing – review & editing, Writing – original draft, Supervision, Methodology, Investigation, Formal analysis, Data curation, Conceptualization.

Declaration of Generative AI and AI-assisted technologies in the writing process

During the preparation of this manuscript the author(s) used ChatGPT in order to improve readability and language of the work. After using this tool, the authors reviewed and edited the content as needed and take full responsibility for the content of the publication.

Declaration of competing interest

The authors declare that they have no known competing financial interests or personal relationships that could have appeared to influence the work reported in this paper.

Appendix A. Supplementary data

Supplementary data to this article can be found online at https://doi.org/10.1016/j.cej.2025.167166.

Data availability

Data will be made available on request.

References

[1] B. Petrovic, M. Gorbounov, S. Masoudi Soltani, Influence of surface modification on selective CO_2 adsorption: a technical review on mechanisms and methods, Microporous Mesoporous Mater. 312 (2021) 110751, https://doi.org/10.1016/j.micromeso.2020.110751.

[2] V. Presser, J. McDonough, S.H. Yeon, Y. Gogotsi, Effect of pore size on carbon dioxide sorption by carbide derived carbon, Energy Environ. Sci. 4 (2011) 3059–3066, https://doi.org/10.1039/c1ee01176f.

[3] A. Vishnyakov, P.I. Ravikovitch, A.V. Neimark, Molecular level models for CO_2 sorption in nanopores, Langmuir 15 (1999) 8736–8742, https://doi.org/10.1021/la990726c.

[4] Z. Zhang, J. Zhou, W. Xing, Q. Xue, Z. Yan, S. Zhuo, S.Z. Qiao, Critical role of small micropores in high CO2 uptake, Phys. Chem. Chem. Phys. 15 (2013) 2523–2529, https://doi.org/10.1039/c2cp44436d.

[5] S. He, G. Chen, H. Xiao, G. Shi, C. Ruan, Y. Ma, H. Dai, B. Yuan, X. Chen, X. Yang, Facile preparation of N-doped activated carbon produced from rice husk for CO_2 capture, J. Colloid Interface Sci. 582 (2021) 90–101, https://doi.org/10.1016/j.jcis.2020.08.021.

[6] S.O. Adio, S.A. Ganiyu, M. Usman, I. Abdulazeez, K. Alhooshani, Facile and efficient nitrogen modified porous carbon derived from sugarcane bagasse for CO_2 capture: experimental and DFT investigation of nitrogen atoms on carbon frameworks, Chem. Eng. J. 382 (2020) 122964, https://doi.org/10.1016/j.cej.2019.122964.

[7] Y. Zhi, J. Shao, C. Liu, Q. Xiao, M. Demir, M.K. Al Mesfer, M. Danish, L. Wang, X. Hu, High-performance CO_2 adsorption with P-doped porous carbons from lotus petiole biomass, Sep. Purif. Technol. 361 (2025) 131253, https://doi.org/10.1016/j.seppur.2024.131253.

[8] Y. Zhi, Y. Yin, Q. Ciren, Q. Xiao, L. Zhao, M. Demir, U.B. Simsek, X. Hu, L. Wang, One-step synthesis of K_3PO_4-activated phosphorus-enriched carbons for enhanced carbon capture, J. Environ. Chem. Eng. 13 (2025) 116694, https://doi.org/10.1016/j.jece.2025.116694.

[9] J. Serafin, B. Dziejarski, P. Rodríguez-Estupiñán, V.B. Fernández, L. Giraldo, J. Sreńscek-Nazzal, B. Michalkiewicz, J.C. Moreno-Piraján, Effective synthesis route of renewable activated biocarbons adsorbent for high CO_2, CH_4, H_2, N_2, C2H4 gas storage and CO_2/N_2, CO_2/CH_4, CO_2/H_2, C_2H_4/CH_4 selectivity, Fuel 374 (2024), https://doi.org/10.1016/j.fuel.2024.132462.

[10] A. Rehman, S.J. Park, From chitosan to urea-modified carbons: tailoring the ultra-microporosity for enhanced CO_2 adsorption, Carbon N. Y. 159 (2020) 625–637, https://doi.org/10.1016/j.carbon.2019.12.068.

[11] L. Rao, R. Ma, S. Liu, L. Wang, Z. Wu, J. Yang, X. Hu, Nitrogen enriched porous carbons from D-glucose with excellent CO_2 capture performance, Chem. Eng. J. 362 (2019) 794–801, https://doi.org/10.1016/j.cej.2019.01.093.

[12] M.A.O. Lourenço, T. Frade, M. Bordonhos, M. Castellino, M.L. Pinto, S. Bocchini, N-doped sponge-like biochar: a promising CO_2 sorbent for CO_2/CH_4 and CO_2/N_2 gas separation, Chem. Eng. J. 470 (2023) 144005, https://doi.org/10.1016/J.CEJ.2023.144005.

[13] Q. Xu, J. Wang, J. Feng, C. Liu, Q. Xiao, M. Demir, U.B. Simsek, M. Kılıç, L. Wang, X. Hu, D-glucose-derived S-doped porous carbon: sustainable and effective CO_2 adsorption, Colloids Surf. A Physicochem. Eng. Asp. 709 (2025) 136054, https://doi.org/10.1016/j.colsurfa.2024.136054.

[14] M. Armandi, B. Bonelli, C.O. Areán, E. Garrone, Role of microporosity in hydrogen adsorption on templated nanoporous carbons, Microporous Mesoporous Mater. 112 (2008) 411–418, https://doi.org/10.1016/j.micromeso.2007.10.017.

[15] M. Armandi, B. Bonelli, K. Cho, R. Ryoo, E. Garrone, Study of hydrogen physisorption on nanoporous carbon materials of different origin, Int. J. Hydrog. Energy 36 (2011), https://doi.org/10.1016/j.ijhydene.2011.01.049.

[16] M. Armandi, B. Bonelli, I. Bottero, C.O. Areán, E. Garrone, Synthesis and characterization of ordered porous carbons with potential applications as hydrogen storage media, Microporous Mesoporous Mater. 103 (2007), https://doi.org/10.1016/j.micromeso.2007.01.049.

[17] R. Wang, P. Wang, X. Yan, J. Lang, C. Peng, Q. Xue, Promising porous carbon derived from celtuce leaves with outstanding supercapacitance and CO_2 capture performance, ACS Appl. Mater. Interfaces 4 (11) (2012) 5800–5806, https://doi.org/10.1021/AM302077C.

[18] O.F. Cruz, I. Campello-Gómez, M.E. Casco, J. Serafin, J. Silvestre-Albero, M. Martínez-Escandell, D. Hotza, C.R. Rambo, Enhanced CO_2 capture by cupuassu shell-derived activated carbon with high microporous volume, Carbon Lett. 33 (2023) 727–735, https://doi.org/10.1007/s42823-022-00454-3.

[19] S. Li, M.K. Cho, S. Deng, J. Wang, K.B. Lee, Upcycling of polyethylene terephthalate waste into porous carbon as potential CO_2 adsorbents through autogenic pressure carbonization, Chem. Eng. J. 494 (2024) 152931, https://doi.org/10.1016/j.cej.2024.152931.

[20] J. Serafin, J. Sreńscek-Nazzal, A. Kamińska, O. Paszkiewicz, B. Michalkiewicz, Management of surgical mask waste to activated carbons for CO_2 capture, J. CO2 Util. 59 (2022), https://doi.org/10.1016/j.jcou.2022.101970.

[21] D. Lozano-Castelló, J.M. Calo, D. Cazorla-Amorós, A. Linares-Solano, Carbon activation with KOH as explored by temperature programmed techniques, and the effects of hydrogen, Carbon N. Y. 45 (2007) 2529–2536, https://doi.org/10.1016/j.carbon.2007.08.021.

[22] P. Ehrburger, A. Addoun, F. Addoun, J.B. Donnet, Carbonization of coals in the presence of alkaline hydroxides and carbonates: formation of activated carbons, Fuel 65 (1986) 1447–1449, https://doi.org/10.1016/0016-2361(86)90121-3.

[23] J. Díaz-Terán, D.M. Nevskaia, J.L.G. Fierro, A.J. López-Peinado, A. Jerez, Study of chemical activation process of a lignocellulosic material with KOH by XPS and XRD, Microporous Mesoporous Mater. 60 (2003) 173–181, https://doi.org/10.1016/S1387-1811(03)00338-X.

[24] C.A. Mims, J.K. Pabst, Role of surface salt complexes in alkali-catalysed carbon gasification, Fuel 62 (1983) 176–179, https://doi.org/10.1016/0016-2361(83)90193-X.

[25] J. Liu, N. Sun, C. Sun, H. Liu, C. Snape, K. Li, W. Wei, Y. Sun, Spherical potassium intercalated activated carbon beads for pulverised fuel CO_2 post-combustion capture, Carbon N. Y. 94 (2015) 243–255, https://doi.org/10.1016/j.carbon.2015.06.036.

[26] R. Xue, Z. Shen, Formation of graphite-potassium intercalation compounds during activation of MCMB with KOH, Carbon 41 (2003) 1862–1864, https://doi.org/10.1016/S0008-6223(03)00161-1.

[27] D. Lozano-Castelló, M.A. Lillo-Ródenas, D. Cazorla-Amorós, A. Linares-Solano, Preparation of activated carbons from Spanish anthracite - I. Activation by KOH, Carbon N. Y. 39 (2001) 741–749, https://doi.org/10.1016/S0008-6223(00)00185-8.

[28] Y. Luo, J. Gong, Z. Yang, Z. Liu, Y. Chen, S. Huang, R. Su, X. Ma, W. Yan, The impact of neglected potassium in KOH-activated porous carbon on CO_2 capture and CO_2/N_2 selectivity: experimental and molecular simulation studies, Appl. Surf. Sci. 681 (2025) 161571, https://doi.org/10.1016/j.apsusc.2024.161571.

[30] G. Nazir, A. Rehman, S.J. Park, Self-activated, urea modified microporous carbon cryogels for high-performance CO_2 capture and separation, Carbon N. Y. 192 (2022) 14–29, https://doi.org/10.1016/j.carbon.2022.02.040.

[31] J. Shao, Y. Wang, C. Liu, Q. Xiao, M. Demir, M.K. Al Mesfer, M. Danish, L. Wang, X. Hu, Advanced microporous carbon adsorbents for selective CO_2 capture: insights into heteroatom doping and pore structure optimization, J. Anal. Appl. Pyrolysis 186 (2025) 106946, https://doi.org/10.1016/j.jaap.2024.106946.

[32] H. Zhang, F. Jiang, X. Zhang, S. Hu, J. Li, H. Zhang, K. Liu, CO_2 adsorption performance of nitrogen-doped activated carbon from banana pseudo-stem by urea-assisted high-pressure CO_2-hydrothermal treatment, Sep. Purif. Technol. 366 (2025) 132773, https://doi.org/10.1016/j.seppur.2025.132773.

[33] Z. Geng, Q. Xiao, H. Lv, B. Li, H. Wu, Y. Lu, C. Zhang, One-step synthesis of microporous carbon monoliths derived from biomass with high nitrogen doping content for highly selective CO_2 capture, Sci. Reports 6 (2016) 1–8, https://doi.org/10.1038/srep30049, 2016 61.

[34] I. Correia, M. Ilkaeva, M. Castellino, S. Bocchini, R.M. Novais, L. Mafra, N.P. F. Gonçalves, M.A.O. Lourenço, Impact of pyrolysis heating methods on biochars with enhanced CO_2/N_2 separation and their incorporation in 3D-printed composites, J. Environ. Chem. Eng. 12 (2024) 113875, https://doi.org/10.1016/j.jece.2024.113875.

[35] J. Chen, J. Yang, G. Hu, X. Hu, Z. Li, S. Shen, M. Radosz, M. Fan, Enhanced CO_2 capture capacity of nitrogen-doped biomass-derived porous carbons, ACS Sustain. Chem. Eng. 4 (2016) 1439–1445, https://doi.org/10.1021/acssuschemeng.5b01425.

[36] L. An, S. Liu, L. Wang, J. Wu, Z. Wu, C. Ma, Q. Yu, X. Hu, Novel nitrogen-doped porous carbons derived from graphene for effective CO_2 capture, Ind. Eng. Chem. Res. 58 (2019) 3349–3358, https://doi.org/10.1021/acs.iecr.8b06122.

[37] L. Yue, Q. Xia, L. Wang, L. Wang, H. DaCosta, J. Yang, X. Hu, CO_2 adsorption at nitrogen-doped carbons prepared by K_2CO_3 activation of urea-modified coconut shell, J. Colloid Interface Sci. 511 (2018) 259–267, https://doi.org/10.1016/J.JCIS.2017.09.040.

[38] L. Yue, L. Rao, L. Wang, L. An, C. Hou, C. Ma, H. Dacosta, X. Hu, Efficient CO_2 adsorption on nitrogen-doped porous carbons derived from d -glucose, Energy Fuel 32 (2018) 6955–6963, https://doi.org/10.1021/acs.energyfuels.8b01028.

[39] J. Shi, H. Cui, J. Xu, N. Yan, Y. Liu, S. Zhang, One-step synthesis of highly porous nitrogen doped carbon from the direct pyrolysis of potassium phthalimide for CO_2 adsorption, J. CO2 Util. 39 (2020) 101164, https://doi.org/10.1016/j.jcou.2020.101164.

[40] M. Armandi, B. Bonelli, F. Geobaldo, E. Garrone, Nanoporous carbon materials obtained by sucrose carbonization in the presence of KOH, Microporous Mesoporous Mater. 132 (2010) 414–420, https://doi.org/10.1016/j.micromeso.2010.03.021.

[41] M.M. Dubinin, Fundamentals of the theory of adsorption in micropores of carbon adsorbents: characteristics of their adsorption properties and microporous structures, Carbon 27 (1989) 457–467, https://doi.org/10.1016/0008-6223(89)90078-X.

[42] M.M. Dubinin, The potential theory of adsorption of gases and vapors for adsorbents with energetically non uniform surfaces, Chem. Rev. 60 (1960) 235–241.

[43] M.M. Dubinin, Adsorption in micropores, J. Colloid Interface Sci. 23 (1967) 487–499, https://doi.org/10.1016/0021-9797(67)90195-6.

[44] A. Nuhnen, C. Janiak, A practical guide to calculate the isosteric heat/enthalpy of adsorption: via adsorption isotherms in metal-organic frameworks, MOFs, Dalton Trans. 49 (2020) 10295–10307, https://doi.org/10.1039/d0dt01784a.

[45] J.M.P.A.L. Myers, Thermodynamics of mixed-gas adsorption, AICHE J. 11 (1965) 121–127.

[46] E. Davarpanah, M. Armandi, S. Hernández, D. Fino, R. Arletti, S. Bensaid, M. Piumetti, CO_2 capture on natural zeolite clinoptilolite: effect of temperature and role of the adsorption sites, J. Environ. Manag. 275 (2020), https://doi.org/10.1016/j.jenvman.2020.111229.

[47] Z.Q. Li, C.J. Lu, Z.P. Xia, Y. Zhou, Z. Luo, X-ray diffraction patterns of graphite and turbostratic carbon, Carbon 45 (2007) 1686–1695, https://doi.org/10.1016/j.carbon.2007.03.038.

[48] M.B. Cerfontain, J.A. Moulijn, The interaction of CO_2 and CO with an alkali carbonate carbon system studied by in-situ Fourier transform infrared spectroscopy, Fuel 65 (1986) 1349–1355, https://doi.org/10.1016/0016-2361(86)90102-X.

[49] J. Wu, S. Ma, J. Sun, J.I. Gold, C. Tiwary, B. Kim, L. Zhu, N. Chopra, I.N. Odeh, R. Vajtai, A.Z. Yu, R. Luo, J. Lou, G. Ding, P.J.A. Kenis, P.M. Ajayan, A metal-free electrocatalyst for carbon dioxide reduction to multi-carbon hydrocarbons and oxygenates, Nat. Commun. 7 (2016) 1–6, https://doi.org/10.1038/ncomms13869.

[50] R. Mishra, P.R. Prasad, P. Panda, S. Barman, Highly porous activated N-doped carbon as an ideal electrode material for capacitive energy storage and physisorption of H_2, CO_2, and CH_4, Energy Fuel 35 (2021) 14177–14187, https://doi.org/10.1021/acs.energyfuels.1c02051.

[51] W. Yu, H. Wang, S. Liu, N. Mao, X. Liu, J. Shi, W. Liu, S. Chen, X. Wang, N, O-codoped hierarchical porous carbons derived from algae for high-capacity supercapacitors and battery anodes, J. Mater. Chem. A 4 (2016) 5973–5983, https://doi.org/10.1039/c6ta01821a.

[52] G.P. Hao, W.C. Li, D. Qian, A.H. Lu, Rapid synthesis of nitrogen-doped porous carbon monolith for CO_2 capture, Adv. Mater. 22 (2010) 853–857, https://doi.org/10.1002/ADMA.200903765.

[53] Á. Sánchez-Sánchez, F. Suárez-García, A. Martínez-Alonso, J.M.D. Tascón, Influence of porous texture and surface chemistry on the CO_2 adsorption capacity of porous carbons: acidic and basic site interactions, ACS Appl. Mater. Interfaces 6 (2014) 21237–21247, https://doi.org/10.1021/AM506176E.

[54] L. Caracciolo, L. Madec, H. Martinez, XPS analysis of K-based reference compounds to allow reliable studies of solid electrolyte interphase in K-ion batteries, ACS Appl. Energy Mater. 4 (2021) 11693–11699, https://doi.org/10.1021/ACSAEM.1C02400. /ASSET/IMAGES/LARGE/AE1C02400_0008.JPEG.

[55] M. Smith, L. Scudiero, J. Espinal, J.S. McEwen, M. Garcia-Perez, Improving the deconvolution and interpretation of XPS spectra from chars by *ab initio* calculations, Carbon N. Y. 110 (2016) 155–171, https://doi.org/10.1016/J.CARBON.2016.09.012.

[56] T. Horikawa, N. Sakao, T. Sekida, J. Hayashi, D.D. Do, M. Katoh, Preparation of nitrogen-doped porous carbon by ammonia gas treatment and the effects of N-doping on water adsorption, Carbon 50 (2012) 1833–1842, https://doi.org/10.1016/j.carbon.2011.12.033.

[57] P. Jagdale, J.R. Nair, A. Khan, M. Armandi, G. Meligrana, F.R. Hernandez, I. Rusakova, E. Piatti, M. Rovere, A. Tagliaferro, M. Winter, C. Gerbaldi, Waste to life: low-cost, self-standing, 2D carbon fiber green Li-ion battery anode made from end-of-life cotton textile, Electrochim. Acta 368 (2021) 137644, https://doi.org/10.1016/j.electacta.2020.137644.

[58] M. Thommes, K.A. Cychosz, Physical adsorption characterization of nanoporous materials: Progress and challenges, Adsorption 20 (2014) 233–250, https://doi.org/10.1007/s10450-014-9606-z.

[59] M. Thommes, K. Kaneko, A.V. Neimark, J.P. Olivier, F. Rodriguez-Reinoso, J. Rouquerol, K.S.W. Sing, Physisorption of gases, with special reference to the evaluation of surface area and pore size distribution (IUPAC technical report), Pure Appl. Chem. 87 (2015) 1051–1069, https://doi.org/10.1515/pac-2014-1117.

[60] J. Garrido, R. Torregrosa, Use of N_2 vs .CO_2 in the characterization of activated carbons, Langmuir 3 (1987) 76–81.

[61] H.F. Stoeckli, J.P. Houriet, The Dubinin theory of micropore filling and the adsorption of simple molecules by active carbons over a large range of temperature, Carbon N. Y. 14 (1976) 253–256, https://doi.org/10.1016/0008-6223(76)90127-5.

[62] D. Cazorla-Amorós, J. Alcañiz-Monge, M.A. De La Casa-Lillo, A. Linares-Solano, CO_2 as an adsorptive to characterize carbon molecular sieves and activated carbons, Langmuir 14 (1998) 4589–4596, https://doi.org/10.1021/la980198p.

[63] Y.S. Bae, R.Q. Snurr, Development and evaluation of porous materials for carbon dioxide separation and capture, Angew. Chem. Int. Ed. 50 (2011) 11586–11596, https://doi.org/10.1002/anie.201101891.

[64] J.S. Bae, S.K. Bhatia, High-pressure adsorption of methane and carbon dioxide on coal, Energy Fuel 20 (2006) 2599–2607, https://doi.org/10.1021/ef060318y.

[65] Y. Zhao, X. Liu, K.X. Yao, L. Zhao, Y. Han, Superior capture of CO_2 achieved by introducing extra-framework cations into N-doped microporous carbon, Chem. Mater. 24 (2012) 4725–4734, https://doi.org/10.1021/cm303072n.

[66] D. Saha, R. Thorpe, S.E. Van Bramer, N. Alexander, D.K. Hensley, G. Orkoulas, J. Chen, Synthesis of nitrogen and sulfur Codoped nanoporous carbons from algae: role in CO_2 separation, ACS Omega 3 (2018) 18592–18602, https://doi.org/10.1021/acsomega.8b02892.

[67] Z. Geng, Q. Xiao, H. Lv, B. Li, H. Wu, Y. Lu, C. Zhang, One-step synthesis of microporous carbon monoliths derived from biomass with high nitrogen doping content for highly selective CO_2 capture, Sci. Rep. 6 (2016) 4–11, https://doi.org/10.1038/srep30049.

[68] Z. Tian, J. Huang, X. Zhang, G. Shao, Q. He, S. Cao, S. Yuan, Ultra-microporous N-doped carbon from polycondensed framework precursor for CO_2 adsorption, Microporous Mesoporous Mater. 257 (2018) 19–26, https://doi.org/10.1016/j.micromeso.2017.08.012.

[69] J.E. Eichler, J.N. Burrow, N. Katyal, G. Henkelman, C.B. Mullins, Modulation of CO_2 adsorption thermodynamics and selectivity in alkali-carbonate activated N-rich porous carbons, J. Mater. Chem. A 11 (2023) 12811–12826, https://doi.org/10.1039/d2ta09376f.

[70] L. Wang, R.T. Yang, Significantly increased CO_2 adsorption performance of nanostructured templated carbon by tuning surface area and nitrogen doping, J. Phys. Chem. C 116 (2012) 1099–1106, https://doi.org/10.1021/jp2100446.

[71] N. Tsubouchi, M. Nishio, Y. Mochizuki, Role of nitrogen in pore development in activated carbon prepared by potassium carbonate activation of lignin, Appl. Surf. Sci. 371 (2016) 301–306, https://doi.org/10.1016/j.apsusc.2016.02.200.

[72] M. Sevilla, G.A. Ferrero, N. Diez, A.B. Fuertes, One-step synthesis of ultra-high surface area nanoporous carbons and their application for electrochemical energy storage, Carbon N. Y. 131 (2018) 193–200, https://doi.org/10.1016/j.carbon.2018.02.021.

[73] J.E. Eichler, J.N. Burrow, Y. Wang, D.C. Calabro, C.B. Mullins, Unraveling porogenesis in nitrogen rich K^+-activated carbons, Carbon N. Y. 186 (2022) 711–723, https://doi.org/10.1016/j.carbon.2021.10.041.

[74] L. Wang, F. Sun, F. Hao, Z. Qu, J. Gao, M. Liu, K. Wang, G. Zhao, Y. Qin, A green trace K_2CO_3 induced catalytic activation strategy for developing coal-converted activated carbon as advanced candidate for CO_2 adsorption and supercapacitors, Chem. Eng. J. 383 (2020) 123205, https://doi.org/10.1016/j.cej.2019.123205.